

# A digital twin solution for floating offshore wind turbines validated using a full-scale prototype

Emmanuel Branlard<sup>1</sup>, Jason Jonkman<sup>1</sup>, Cameron Brown<sup>2</sup>, and Jiatian Zhang<sup>2</sup>

<sup>1</sup>National Renewable Energy Laboratory, Golden, CO 80401, USA

<sup>2</sup>Stiesdal Offshore A/S, Denmark

**Correspondence:** E. Branlard (emmanuel.branlard@nrel.gov)

1 **Abstract.** In this work, we implement, verify, and validate a physics-based digital twin solution applied to a floating offshore  
2 wind turbine. The digital twin is validated using measurement data from the full-scale TetraSpar prototype. We focus on the  
3 estimation of the aerodynamic loads, wind speed, and section loads along the tower, with the aim ~~at~~-of estimating the fatigue  
4 lifetime of the tower. Our digital twin solution integrates ~~:-~~1) a Kalman filter to estimate the structural states based on a  
5 linear model of the structure and measurements from the turbine, 2) an aerodynamic estimator, and 3) a physics-based virtual  
6 sensing procedure to obtain the loads along the tower. The digital twin relies on a set of measurements that are expected to be  
7 available on any existing wind turbine (power, pitch, rotor speed, and tower acceleration), and motion sensors that are likely  
8 to be standard measurements for a floating platform (inclinometers and GPS sensors). We explore two different pathways  
9 to obtain physics-based models: a suite of dedicated Python tools implemented as part of this work ~~, or~~-and the OpenFAST  
10 linearization feature. In our final version of the digital twin, we use components from both approaches. We perform different  
11 numerical experiments to verify the individual models of the digital twin. In this simulation realm, we obtain estimated damage  
12 equivalent loads with an accuracy of ~~the order of~~-approximately 5% to 10%. When comparing the digital twin estimations with  
13 the measurements from the TetraSpar prototype, the errors increased to 10%–15% on average. Overall, the accuracy of the  
14 results ~~appears~~-is promising and demonstrates the possibility ~~to use~~-of using digital twin solutions to estimate fatigue loads  
15 on floating offshore wind turbines. A natural continuation of this work would be to implement the monitoring and diagnostics  
16 aspect of the digital twin ~~, to~~-inform operation and maintenance decisions. The digital twin solution is provided with examples  
17 as part of an open-source repository.

## 18 1 Introduction

19 The offshore floating wind turbine market is expected to grow in the ~~next coming~~ decades as the technology ~~is gaining~~-gains  
20 in maturity, with several floating wind turbine prototypes already tested and commissioned, such as the TetraSpar, developed  
21 by Stiesdal Offshore (Stiesdal Offshore, 2022). Operation ~~&~~-and maintenance (O&M) costs can account for approximately  
22 one-third of offshore wind farm life cycle expenditures for a fixed-bottom project and are expected to be higher for remote  
23 (floating) projects (Castella, 2020). Reducing the O&M costs is therefore an impactful and effective means to lower the costs  
24 of floating offshore projects. Digital twin solutions are increasingly being ~~considered~~-used to follow products during their life

25 cycle to assess component conditions, guide predictive maintenance, and thereby reduce O&M costs. A review of digital twins  
26 for power systems is found in Song et al. (2023). Digital twins often include a virtual sensing component ~~whose role consists~~  
27 ~~of providing information that are that provides information~~ not measured by the physical system, and a structural health moni-  
28 toring component to assess the condition of the system. Virtual sensing technology is usually achieved using physics-based or  
29 data-driven approaches; both approaches relying on measurements from the physical system to infer and extrapolate informa-  
30 tion about its current state. Physics-based approaches use a numerical model of the system, whereas data-driven approaches  
31 ~~either use ad-hoc use either ad hoc~~ algorithms or machine-learning techniques. ~~Machine-learning approaches can be trained~~  
32 ~~using high-fidelity models or measurements, leading to potentially high accuracies while maintaining low computational time,~~  
33 ~~but their training requirements imply that a technology cannot be readily transferred from one platform to another.~~ Physics-  
34 ~~based models often require low-fidelity models to achieve computational times low enough for digital twins to run in real time.~~  
35 ~~They nevertheless offer the advantage that they provide tractable and insightful results, and, they can be applied to a same~~  
36 ~~family of wind turbine concepts because they do not require a training dataset. Currently, there is no definite case as to which~~  
37 ~~approach can lead to the best digital twin implementation, and it is possible that future approaches will combine physics-based~~  
38 ~~with data-driven techniques.~~ This work presents the development, verification, and validation of a physics-based digital twin  
39 for floating wind turbines ~~as a proof of concept for future maturation of the technology.~~

40 Digital twins for wind turbine applications have recently become a topic of research interest. The ~~current~~ authors explored the  
41 topic of physics-based digital twins in previous work, ~~where in which~~ a method to estimate tower loads on land-based turbines  
42 was developed (Branlard et al., 2020a, b). The approach relied on a Kalman filter model (Kalman, 1960; Zarchan and Musoff,  
43 2015) ~~that combines a linear physics-based model of the structure with measurements from the turbine to perform a virtual~~  
44 ~~sensing of the tower section loads and estimate the fatigue of this component.~~ The measurement data ~~was were~~ taken from the  
45 supervisory control and data acquisition (SCADA) system using sensors readily available on most turbines. The approach used  
46 a mix between an augmented Kalman filter approach (Lourens et al., 2012), where the loads are estimated with the states of the  
47 system, and a physics-based aerodynamic estimator for aerodynamic thrust. Bilbao et al. (2022) used a Gaussian process latent  
48 force model ~~instead~~ to estimate the forcing of the system ~~and thereby obtain the section loads along the tower.~~ Drivetrains  
49 are another component ~~that has recently been an application of digital twin for which a digital twin has been applied,~~ with  
50 physics-based approaches presented ~~for instance in (Mehlan et al., 2022, 2023)~~ in Mehlan et al. (2022, 2023), and data-driven  
51 models ~~presented~~ in Kamel et al. (2023).

52 ~~In spite~~ ~~Despite the recent popularity~~ of the term “digital twin” ~~becoming recently popular, it,~~ ~~the concept~~ is heavily based on  
53 the fields of ~~structural health~~ structural health monitoring and load estimations (or more generally, virtual sensing), which have  
54 long been topics of research. For instance, Iliopoulos et al. (2016) used physics-based modal decomposition to estimate the dy-  
55 namic response on the substructure of a fixed-bottom wind turbine. Neural networks have been used to establish transfer func-  
56 tions or surrogate models based on SCADA data to obtain wind turbine loads with the aim of performing conditional monitor-  
57 ing (see, e.g., Cosack (2010); Schröder et al. (2018)). Kalman filters were introduced in fields other than wind energy to perform  
58 load estimation, ~~for instance in the following references: Auger et al. (2013); Ma and Ho (2004); Eftekhar Azam et al. (2015); Lourens et al.~~  
59 ~~(Auger et al., 2013; Ma and Ho, 2004; Eftekhar Azam et al., 2015; Lourens et al., 2012).~~ Kalman filtering has been extensively

60 used in wind energy to estimate rotor loads and improve wind turbine control ~~see, e.g., Boukhezzar and Siguerdidjane (2011); Selvam et al.~~  
61 ~~-(Boukhezzar and Siguerdidjane, 2011; Selvam et al., 2009; Bottasso and Croce, 2009; Bossanyi, 2003)~~. Load estimations were  
62 also achieved using ~~hybrid-techniques~~ hybrid techniques combining physics based on SCADA data by Noppe et al. (2016).  
63 Other load estimation techniques may be used, such as lookup tables (Mendez Reyes et al., 2019), modal expansion (Iliopoulos  
64 et al., 2016), machine learning (Evans et al., 2018), neural networks (Schröder et al., 2018), polynomial chaos expansion (Dim-  
65 itrov et al., 2018), deconvolution (Jacquelin et al., 2003), or load extrapolation (Ziegler et al., 2017).

66 In this work, we build on our previous work related to fixed-bottom turbines and present a digital twin solution for floating  
67 wind turbines that relies on physics-based models and a Kalman filter. We apply the digital twin to the TetraSpar structure and  
68 use measurements from the full-scale prototype. Achieving computational efficiency is crucial to be able to run the digital twin  
69 online, therefore, a reduced order model with few selected degrees of freedom is used. Developing digital twins for floating  
70 wind turbines present a set of challenges compared to our previous work on fixed-bottom foundations. The potentially large  
71 motions undergone by the platform may affect the aerodynamics and accelerometer signals. The models developed for fixed-  
72 bottom foundations need to be augmented to be able to predict the aerodynamics when the platform experiences large pitching  
73 motions. The dynamics of the platform motion needs to be well captured for the tower-top accelerometer to be used and for  
74 estimating the loading in the stationkeeping system. In both floating and fixed-bottom wind turbines, hydrodynamic loads need  
75 to be estimated to capture member-level loads in the substructure but they can be omitted as a first approximation if only the  
76 tower loads are estimated, as in this study.

77 In Section 2, we provide an overview of our digital concept, the vision for future application, and the TetraSpar prototype on  
78 which the digital twin is applied. In Section 3, we present the individual components of the digital twin, and run some isolated  
79 verification studies on them. In Section 4, we present results from the digital twin application first using numerical experiments,  
80 and then using measurements from the TetraSpar prototype before concluding. To avoid lengthening the main text, we provide  
81 derivations (some being of which are important contributions of this work) and additional results in appendices.

## 82 2 Overview of the digital twin concept

83 In this section, we provide an overview of our digital twin concept and how it is applied in this study.

### 84 2.1 Long-term vision of the digital twin concept

85 Many definitions and applications of digital twins are possible. The vision for the concept discussed in ~~the~~ this work is to  
86 follow the life cycle of a wind turbine in ~~real-time~~ real time and ultimately provide tangible signals to inform O&M decisions.  
87 Our goal is to achieve this by relying only on measurements expected to be available on most wind turbines, thereby avoiding  
88 the extra cost of adding sensors. In this work, we leave open the question as to whether the installation of an additional set of  
89 optimally placed and selected sensors can further improve the predictions of the digital twin, further reducing the long-term  
90 O&M costs, and thereby warranting the additional costs of adding the sensors.

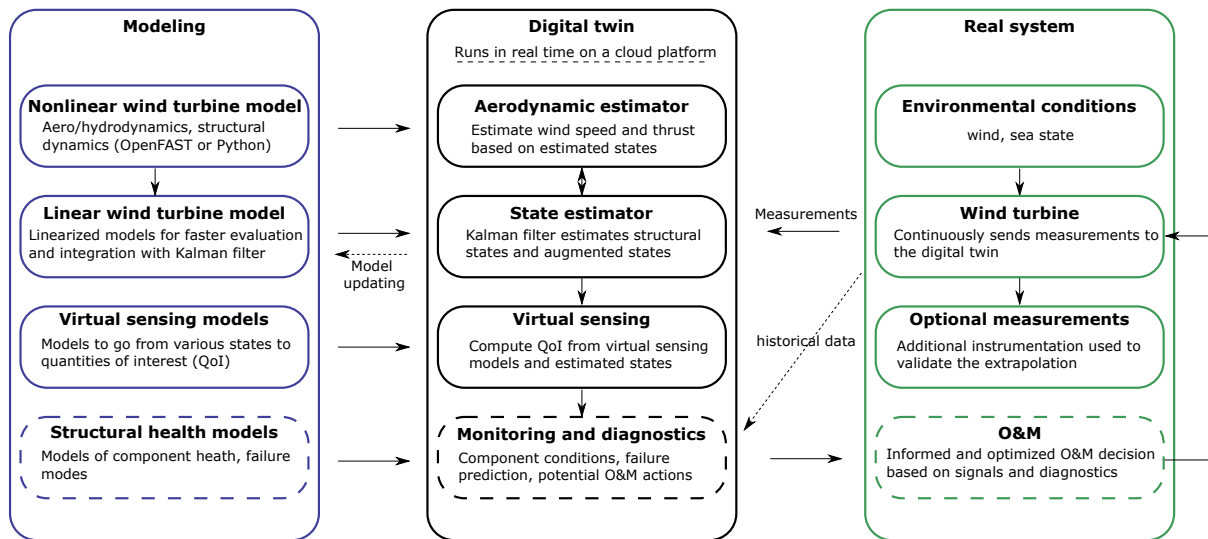


**Figure 1.** Overview of the digital twin concept. ~~Dashes~~ Dashed lines indicate features that are outside the current scope.

91 We illustrate our approach and vision in Figure 1. The digital twin is intended to run in ~~real-time~~ real time on a cloud  
 92 platform. It combines a set of models (on the left of the figure) with data from the real system (on the right) to perform the  
 93 estimation of various states and eventually produce diagnostics that can be use to inform the O&M. The data from the real  
 94 system are taken from high-frequency measurements from the SCADA system (e.g., power, pitch, rotor speed). The states  
 95 estimated by the digital twin include aerodynamic states (wind speed, thrust) and motions of the structure (e.g., surge, pitch,  
 96 tower deflection). The core algorithm in the estimation is a Kalman filter that uses a linear wind turbine model. The estimated  
 97 states are used in ~~an~~ a “virtual sensing” step ~~,~~ to produce quantities of interests (QoI), such as the loads at key locations of the  
 98 structure. The QoI are then intended to be postprocessed by a monitoring and diagnostic tool to generate the data needed to  
 99 perform condition-based O&M.

## 100 2.2 Narrowed scope

101 The boxes in Figure 1 ~~that are surrounded with dashes are not addressed in the current work, namely: the structural~~ with dashed-  
 102 line borders—structural health modeling, monitoring and diagnostics, and O&M ~~decisions. These decisions—are postponed to~~  
 103 future work, even though they are essential steps ~~necessary~~ to achieve our final vision, ~~but they are postponed to future work.~~  
 104 Dashed lines ~~indicate possible~~ and arrows indicate options that may be exploited in the future but are also outside of our scope:  
 105 the use of historical data to assist in the diagnostics, the use of estimates to perform ~~modeling~~ model updating, and real-time  
 106 implementation.

107 This work therefore focuses on the estimation of states and environmental conditions under the assumption that the estimated  
 108 quantities can replace costly measurements and eventually be used for O&M decisions. We intend to provide a proof of concept

109 ~~paving that paves~~ the way for future commercial applications. A detailed description of each of the boxes surrounded with ~~plain~~  
110 ~~lines will be provided~~ solid lines is given in Section 3.

## 111 2.3 System studied

### 112 2.3.1 The TetraSpar prototype

113 ~~Throughout this article, the system studied~~The system studied for this article is the TetraSpar floating offshore prototype. The  
114 system consists of a floating platform and ~~station-keeping~~ stationkeeping system developed by Stiesdal Offshore in collabo-  
115 ration with partners Shell, RWE, and TEPCO Renewable Power, and a 3.6-MW wind turbine with a rotor diameter of 130 m  
developed by Siemens Gamesa Renewable Energy. A sketch of the system is provided in Figure 2. The prototype was installed

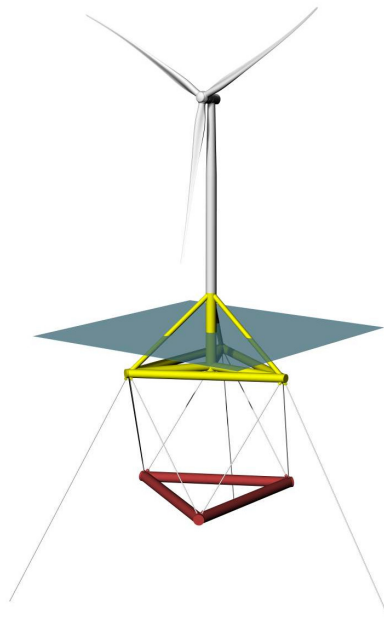


**Figure 2.** Sketch of the TetraSpar prototype

116  
117 off the coast of Norway and commissioned in November 2021. The prototype turbine is equipped with additional sensors  
118 (labeled “Optional measurements” in Figure 1), which we ~~will~~ use to validate the estimated QoI.

### 119 2.3.2 Numerical experiments

120 Prior to using measurement data, we ~~will~~ use simulations (referred to as “numerical experiments”) in place of the real system to  
121 ~~feed-in-feed~~ data to the digital twin. The advantage of this approach is that the QoI are directly accessible and can be compared  
122 to the estimates for verification purposes.

123 Data for the numerical experiments ~~is~~ are obtained using OpenFAST simulations (Jonkman et al., 2023). A model of the  
 124 TetraSpar floating platform and the wind turbine was implemented in OpenFAST based on data provided by the manufactur-  
 125 ers. ~~The~~ All the members of the substructure are modelled using the strip-theory approach (Morison equation) because the  
 126 inherent long-wavelength assumption of the strip-theory has been shown to be sufficiently accurate for this structure with rel-  
 127 atively slender members. The OpenFAST model is complemented with NREL’s Reference OpenSource Controller (ROSCO,  
 128 Abbas et al. (2021)). The controller parameters are tuned so that OpenFAST simulations match the operating conditions of the  
 129 turbine ~~were~~ extracted from SCADA data (pitch, rotor speed and power). The nacelle velocity feedback option of ROSCO is  
 130 used to reduce the platform pitching motion. Using trial and error, the frequency and damping ratio of the pitch PI-controller  
 131 are set to  $\omega_p = 0.05$  rad/s and ~~a controller was tuned to approximate these conditions.~~  $\zeta_p = 7\%$ , and the values for the  
 132 torque controller are set  $\omega_Q = 0.15$  rad/s and  $\zeta_Q = 7\%$ . The gain-scheduling of the pitch controller are obtained using the  
 133 tuning feature of ROSCO. We note that the controller is only needed to perform verifications of the digital twin with real-  
 134 istic time series of the turbine responses, but the controller itself is not used for the design of the digital twin. We use the  
 135 following modules of OpenFAST (~~see, and Jonkman et al. (2023)~~) (Jonkman et al., 2023): MAP (mooring lines), HydroDyn  
 136 (hydrodynamics), ElastoDyn (tower and blade elasticity; rigid floater), AeroDyn (aerodynamics), InflowWind (wind inflow),  
 137 and ServoDyn (controller interface).

138 For the numerical experiments, we use synthetic turbulent wind fields generated using TurbSim (~~Jonkman and Buhl (2006)~~  
 139 ) (Jonkman and Buhl, 2006). In particular, we ~~will~~ often use the same wind field, ~~that we will~~ which we refer to as the “turbulent  
 140 step”, where a deterministic ramp and drop are added to a turbulent field. The advantage of this 10-min wind field is that ~~is~~  
 141 it covers all the operating regions of the turbine in a challenging way because the variations of the wind speed are sudden. The  
 142 wind speed at hub height for the turbulent step can be seen in Figure 6.

### 143 2.3.3 Main aspects of the structural model

144 We model the structure using a set of 8 degrees of freedom (~~DOFs~~ DOF), as illustrated in Figure 3. The platform is repre-  
 145 sented as a rigid body, and its motion is described using 6 ~~DOFs~~ DOF: surge, sway, heave, roll, pitch, and yaw, respectively  
 146 noted  ~~$x, y, z, \phi_x, \phi_y, \phi_z$~~   $x, y, z, \phi_x, \phi_y, \phi_z$ . The tower bending in the fore-aft direction is represented using ~~one~~ 1 gen-  
 147 eralized DOF,  $q_t$ , associated with a Rayleigh-Ritz shape function, taken as the first fore-aft mode shape of the tower (~~see,~~  
 148 ~~e. g., Branlard (2019)~~) (Branlard, 2019). The shape function along the tower height,  $z_t$ , is written as  $\Phi(z_t)$ , with  $\Phi(0) = 0$   
 149 at the tower bottom, and  $\Phi(L_T) = 1$  at the tower top, where  $L_T$  is the tower length. The shaft rotation is noted  $\psi$ , so that  
 150 the rotation speed of the rotor is  ~~$\dot{\psi}$  where the dotted,~~ where the dot notation indicates differentiation with respect to time.  
 151 The ~~rotor-nacelle-assembly (RNA)~~ rotor-nacelle assembly is modeled as a rigid body. The full vector of ~~DOFs is therefore:~~  
 152  ~~$\mathbf{q} = [x, y, z, \phi_x, \phi_y, \phi_z, q_t, \psi]$~~  DOF is therefore  $\mathbf{q} = [x, y, z, \phi_x, \phi_y, \phi_z, q_t, \psi]$ . The equations of motion will be recast into a  
 153 first-order form by concatenating the vector of ~~DOFs~~ DOF and its time derivative,  $\mathbf{x} = [\mathbf{q}, \dot{\mathbf{q}}]$ . The selected set of DOF capture  
 154 the first-order effects as it is the minimal set required to capture the full motion of the floater (necessary to compute restoring  
 155 loads and tower loads), the tower flexibility (necessary to capture tower loads) and the rotor motion (necessary to capture the  
 156 aerodynamics). Additional degrees of freedom could be considered to increase the modeling accuracy, in particular to include

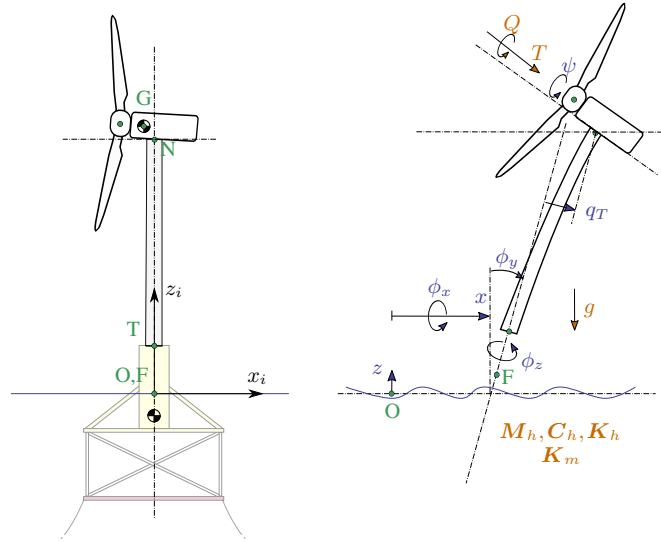


**Figure 3.** Notations for the structural modeling of the floating wind turbine, assuming no yawing of the nacelle. Left: main points ( $F, T, N, O, G$ ) and inertial coordinate system ( $i$ ). Right: degrees of freedom ( $x, y, z, \phi_x, \phi_y, \phi_z, q_t, \psi$ ) and main loads: aerodynamics ( $T, Q$ ), hydrodynamics ( $6 \times 6$  mass and damping and stiffness matrices,  $M_h, C_h, K_h$ —Wave; wave excitation force neglected), mooring ( $6 \times 6$  stiffness matrix,  $K_m$ ), and gravity ( $g$ ).

157 floater flexibility for internal calculation of substructure member loads. This would increase the computational requirement  
 158 and only contribute to second-order effects, and it is therefore postponed to future work.

159 In this work, we perform a simplifying assumptions, e.g., neglecting the influence of nacelle yaw on the system. The mea-  
 160 surement data is are conveniently provided in the fore-aft and side-side system of the nacelle. The main assumption is therefore  
 161 that we assume a rotational symmetry of the platform and mooring system about the yaw axis. We intend to lift this assumption  
 162 in future work. Some of the consequences of this assumption is that we do not capture changes of inertial properties due to  
 163 asymmetry of the support structure and changes of stiffness of the mooring system. In the case of the TetraSpar, the mass  
 164 matrix of the floater does not vary significantly with the yawing of the coordinate system, and the assumption appears fair.  
 165 For the restoring stiffness of the mooring system, the diagonal terms do not vary significantly as the coordinate system yaws,  
 166 but some of the coupling terms vary by 50% to 200%. The couplings between the platform DOF are likely wrongly estimated  
 167 under the rotational symmetry assumption. The impact is nevertheless limited because most of the platform DOF ( $x, y, \phi_x$ , and  
 168  $\phi_y$ ) are measured and therefore observable by the Kalman filter.

### 169 3 Individual components of the digital twin

170 In this section, we describe and verify the individual components of the digital twin presented in Figure 1. In Section 4, we  
 171 will present applications of the digital twin where all the individual components are combined together.

## 172 3.1 Wind turbine measurements

The measurements used as inputs to the digital twin are listed in Table 1. These outputs are stored in a database at a sampling

**Table 1.** Measurements used as inputs to the digital twin.

Signal	Symbol
<del>Blade</del> Collective blade pitch angle	$\theta_p$
Rotor speed	$\dot{\psi}$
Generator torque*	$Q_g$
<del>Surge and Sway</del> Platform surge and sway	$x, y$
<del>Roll and Pitch</del> Platform roll and pitch	$\phi_x, \phi_y$
Nacelle accelerations	$\ddot{\mathbf{r}}_N$

\* Obtained from the power measurement using Equation 2.

173

174 rate of 25 Hz. We expect these measurements to be standard sensors for any floating wind turbine. The TetraSpar prototype is  
175 equipped with additional measurements that ~~will be~~ are used to validate the implementation of the digital twin (see Section 4).

## 176 3.2 Nonlinear wind turbine models

### 177 3.2.1 Overview

178 Similar to our previous work (Branlard et al., 2020b), we use two different pathways to obtain nonlinear and linear models of  
179 floating wind turbines: OpenFAST and WELIB (Wind Energy LIBrary, Branlard (2023b)). The ~~different modeling approaches~~  
180 ~~are illustrated in~~ OpenFAST approach was described in Section 2.3.2, it is compared to the WELIB approach in Table 2 and  
181 ~~further presented below~~. the WELIB toolset is further discussed below. In the next sections, we will show that the results from  
182 both approaches are consistent with each other so that either of the two can be used to obtain nonlinear and linear reduced  
183 order models. Ultimately, in Section 4, a mix of the two approaches is used for the digital twin: linear OpenFAST models for  
184 the state-space equations (Section 3.5) and WELIB for the virtual sensing step (Section 3.6).

185 ~~The OpenFAST approach was described in . The~~

### 186 3.2.2 WELIB tools

187 The WELIB approach consists of a set of dedicated open-source Python tools that are similar to the ElastoDyn, HydroDyn  
188 and MAP modules of OpenFAST. We developed ~~this Python code~~ these tools to offer additional modularity and granularity;  
189 ~~for instance to allow for~~: the tools can be called individually or together; their states, inputs and outputs can be accessed and  
190 manipulated at each time step; and the Python scripting eases the manipulation of the models. For instance, this allows for: 1)  
191 analytical linearization of the structural dynamics, 2) simple linearization of the hydrodynamics (obtention of ~~6x6~~  $6 \times 6$  ma-  
192 trices), 3) linearization of hydrodynamics with respect to wave elevation, 4) linearization with respect to parameters (Jonkman  
193 et al., 2022), and 5) interactive time-stepping of the linear and nonlinear ~~models. One shortcoming is that WELIB does not~~



**Table 2.** Approaches and tools used to obtain nonlinear and linear models.

Approach	Tool	Usage	Formulation & Linearization
1 OpenFAST	OpenFAST (ElastoDyn, HydroDyn, MAP, AeroDyn)	Structural model Hydrodynamics Mooring Aerodynamics Virtual sensing	Numerical and analytical
2 WELIB (Python tools)	YAMS	Structural model Virtual sensing	Analytical
	pHydroDyn	Hydrodynamics	Numerical
	pyMAP	Mooring	Numerical

194 ~~cover the full range of options available with OpenFAST, which is a continuously evolving, extensively verified and validated~~  
 195 ~~tool~~-model. In this work, we mostly use the first two features listed above and their usage will be described in Section 3.3.2. Re-  
 196 sults from time-stepping simulations will be presented in Section 3.3.3. We expect to exploit the additional features of WELIB  
 197 in future digital-twin implementations. For this work, we implemented the following tools in WELIB: 1) YAMS, a symbolic  
 198 structural dynamics package to obtain the equations of motion of an assembly of rigid and flexible bodies analytically, and  
 199 allow for their analytical linearization (Branlard and Geisler, 2022); 2) pHydroDyn, a Python version of the module Hydro-  
 200 Dyn (with a subset of HydroDyn’s functionality) to determine the hydrodynamic loads; and 3) pyMAP, a wrapper around the  
 201 MAP module of OpenFAST, to obtain the mooring quasi-statics. With these three additions, it is possible to perform nonlinear  
 202 simulations of floating wind turbines using WELIB and perform comparisons with OpenFAST. ~~The benefits of-~~

### 203 3.2.3 Differences between the two nonlinear approaches

204 Currently, no controller or aerodynamic module is present in WELIB. Therefore, nonlinear timestepping simulations with  
 205 WELIB are limited to free-decay simulations or prescribed loads. Another shortcoming is that WELIB does not cover the full  
 206 range of options available with OpenFAST, which is a continuously evolving, extensively verified and validated tool. Such  
 207 options include the potential flow representation of hydrodynamic bodies, the flexibility of the floating structure, aerodynamic  
 208 and control features. One benefit of WELIB over OpenFAST is the possibility to perform interactive time-stepping, that is,  
 209 to change the states and inputs dynamically during the simulation. We do not use this approach in this work, but it can be  
 210 considered for nonlinear digital twin applications, for instance, using an extended Kalman filter algorithm. Another benefit  
 211 is the possibility to obtain analytical linear models ~~and~~ of the structure, which avoids using finite-differences and therefore  
 212 reduces the associated numerical errors. In the WELIB approach, the individual modules are linearized separately before being  
 213 combined into the final linear model, and it is therefore easier to understand where each term in the Jacobians of the linear  
 214 models comes from, and thereby, gain physical intuitiveness on the model. ~~Results~~-Ultimately, the linear models obtained by  
 215 both approaches are similar and differ mostly based on differences in the structural dynamics equations and the implementation

216 of rotational transformation matrices. Results comparing time simulations using both approaches will be presented in see  
217 Section 3.3.

### 218 3.3 Linear wind turbine models

219 As part of our digital twin concept, we have chosen to use linear wind turbine models and a Kalman filter for the core of the  
220 state estimation (see Section 3.5). Nonlinear models and an extended Kalman filter could be considered in future iterations. In  
221 this section, we describe how the linear models from OpenFAST and WELIB are obtained.

#### 222 3.3.1 OpenFAST linearization

223 OpenFAST can provide full-system linearization of its underlying nonlinear models by using a mix of ~~analytically- and finite~~  
224 ~~difference-derived-analytically and finite-difference-derived~~ Jacobians (Jonkman and Jonkman, 2016; Jonkman et al., 2018).  
225 The linearization process provides the state-space model ( $\delta\dot{x} = A\delta x + B\delta u$ ) and output equation ( $\delta y = C\delta x + D\delta u$ ) for  
226 small perturbations (indicated with  $\delta$ ) of the internal states ( $x$ ), inputs ( $u$ ), and outputs ( $y$ ) of OpenFAST, around ~~the-linearized~~  
227 ~~a selected~~ operating point. OpenFAST provides the linear model for the entire set of states, inputs, and outputs present in the  
228 model (including virtual sensor-type outputs typically written to an output file and not used internally). In this work, we extract  
229 subsets of the  $A$ ,  $B$ ,  $C$ , and  $D$  matrices and combine them to form the linear model of the state estimator (see Section 3.5).

#### 230 3.3.2 WELIB linearization

231 WELIB performs the linearization of the structure, hydrodynamics, and moorings independently, before combining them into  
232 one model. The aerodynamic loads are not linearized because a dedicated aerodynamic estimator is used in this work (see  
233 Section 3.4). The steps are as follows:

- 234 – The structural equations are linearized analytically using our symbolic framework (Branlard and Geisler, 2022). We  
235 ~~introduce-introduced~~ a notion of “augmented inputs” to linearize the equations of motion without an explicit knowledge  
236 of the external forces. The process is described in Appendix A.
- 237 – We compute the  $6 \times 6$  linearized rigid-body hydrodynamics matrices (mass matrix  $M_h$ , damping matrix  $C_h$ , and stiffness  
238 matrix  $K_h$ ) corresponding to the six rigid-body motions of the platform. ~~We obtain them using numerical differentiation~~  
239 ~~in two different ways~~At the time of this study, these matrices could not be obtained directly from OpenFAST. While  
240 working on this issue, we ended up devising multiple ways to obtain them. They can now be obtained using: 1) using  
241 ~~the full-system linearization of the HydroDyn module~~, 2) the Python implementation of the HydroDyn module by per-  
242 forming rigid-body ~~perturbation-perturbations~~ of the full platform, or ~~2) using~~ 3) an upgraded version of the OpenFAST  
243 HydroDyn driver that also uses rigid-body perturbations. The first approach uses baseline OpenFAST functionalities but  
244 requires additional postprocessing scripts and derivations. The full-system ~~linearization of the HydroDyn module~~. The  
245 ~~latter-linearization of OpenFAST~~ provides Jacobians of the hydrodynamic loads as a function of motions of the individual  
246 hydrodynamic analysis nodes (of which models often have hundreds to thousands of). To transfer these individual Jaco-

247 bians to the reference point and obtain the  $6 \times 6$  matrices, we developed and used the method presented in Appendix B.  
 248 The process is involved and prone to errors. In comparison, the second and third approaches are straightforward to im-  
 249 plement and are several orders of magnitude faster. The Python version was implemented first and then ported over  
 250 to Fortran so that it can be readily available to the OpenFAST community. The consistency between the ~~two~~-different  
 251 approaches was verified. ~~The~~, and because of its ease of use, the second approach is ~~not straightforward to implement,~~  
 252 ~~therefore, we upgraded the OpenFAST HydroDyn driver to provide the  $6 \times 6$  hydrodynamic matrices directly without~~  
 253 ~~the need to use the full-system linearization~~. retained in this study. We note that in this study, all members are modeled  
 254 using the Morison equation and the hydrodynamic drag is set to zero during the linearization process. There is therefore  
 255 no frequency-dependent damping, and the effect of hydrodynamic drag is assumed to be part of the modeling uncertainty  
 256 of the state estimator (see Section 3.5).

257 – The linearized  $6 \times 6$  mooring stiffness matrix,  $\mathbf{K}_m$ , is obtained by calling the linearization feature of the MAP module,  
 258 and transferring the Jacobian to the reference point using the method outlined in Appendix B.

259 – The linearized equations of motion are assembled as:

$$260 \quad [M_0 + Q_0 M_h] \delta \ddot{\mathbf{q}} + [C_0 + Q_0 C_h] \delta \dot{\mathbf{q}} + [K_0 + Q_0 (K_h + K_m)] \delta \mathbf{q} = \delta \mathbf{f}_a + \delta \mathbf{f}_h \quad (1)$$

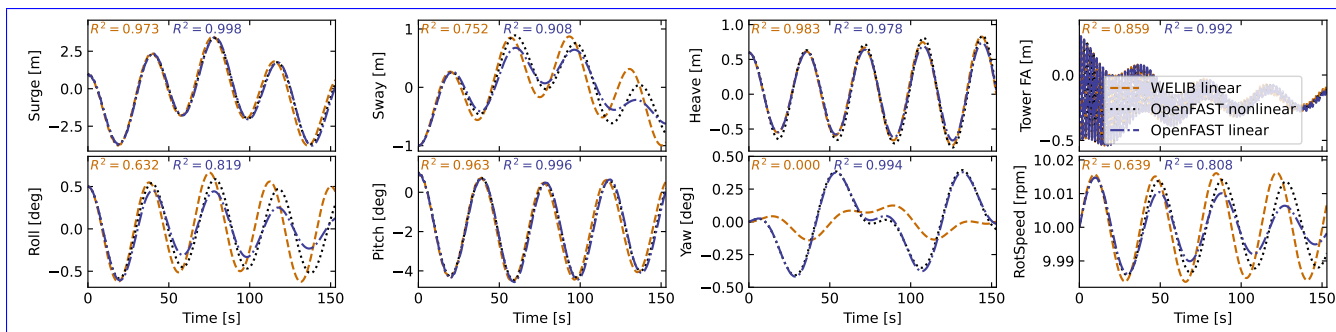
261 where the matrices with subscript 0 originate from the linearization of the structure (see Appendix A). The ~~term~~-matrix  
 262  $Q_0$  ~~is used here to map the~~, of dimension  $8 \times 6$ , maps the subset of the 6 rigid-body platform ~~degrees of freedom~~-DOF  
 263  $(x, y, z, \phi_x, \phi_y, \phi_z)$ , used for the definitions of  $M_h$ ,  $C_h$ ,  $K_h$  and  $K_m$ , to the full vector of ~~degrees of freedom~~-DOF,  $\mathbf{q}$ .  
 264 The term  $\delta \mathbf{f}_a$  is an approximation of the aerodynamic loads, and will be discussed in Section 3.4. The term  $\delta \mathbf{f}_h$  is an  
 265 approximation of the hydrodynamic wave-excitation loads ~~and it will be~~. In this work,  $\delta \mathbf{f}_h$  is mapped into the inherent  
 266 model noise of the Kalman filter ~~in~~ (see Section 3.5). Assuming that the loading is part of the model noise is a crude  
 267 approximation that is expected to be fair as long as the loading has a zero mean value, which is expected to be the  
 268 case for the wave loading, but not for the wind or current loading (here omitted). This modeling choice is not very  
 269 influential in this work because the motions of the platform measured by the inclinometers and GPS sensors inherently  
 270 carry information about the wave loading. Improvements could be obtained by including a model for the wave-excitation  
 271 loads, and further, limiting the wave load signal such that it remains within a certain frequency band.

272 For instance, we could introduce a hydrodynamic state analog to the wave elevation or a set of states that scales different  
 273 hydrodynamic shape functions so that the hydrodynamic load can be obtained as a linear superposition of scaled shape  
 274 functions. In our application (tower section loads), such modeling did not appear necessary, but it will be considered in  
 275 future work as it can be relevant to estimate substructure loads.

276 – We recast Equation 1 into a first-order system to obtain the state matrix  $\mathbf{A}$ .

278 In this section, we compare results from the OpenFAST nonlinear model, the OpenFAST linear model, and the WELIB linear  
 279 model  $\bar{\tau}$  for free-decay simulations of the TetraSpar structure. Free-decay simulations are sufficient because wave and aerody-  
 280 namic loads are purposely not included in the linear models used by the digital twin. The OpenFAST linear model is obtained  
 281 about the operating point defined by  $\mathbf{q}_0 = \mathbf{0}$  and  $\dot{\psi}_0 = 10$  rpm. All models (including the OpenFAST nonlinear model) use  
 282 8 DOFs/DOF. The initial conditions are set to  $\mathbf{q} = [1, -1, 0.6, 0.5, 0.5, 0, -0.2, 0]$   $\mathbf{q} = [1, -1, 0.6, 0.5, 0.5, 0, -0.2, 0]$  (in m and  
 283 deg) and  $\dot{\psi} = 10$  rpm, after which the structure is free to decay/move.

284 First, simulation without hydrodynamics (structure only) are considered, to isolate and verify the structural-dynamics part  
 285 of the models. The time responses from the linear and nonlinear models are in strong agreement when only the structure is  
 286 considered (see results in Appendix C). Below, we present Then, we consider results for a model that includes hydrodynamics  
 287  $\bar{\tau}$  but without wind or external waves (still water). Free decay of the structure using nonlinear and linear models for a case  
 288 including moorings and hydrodynamics (still water). Time-series of the main DOFs. We set the hydrodynamic drag to zero  
 289 due to the difficulty in linearizing this term and will let the state estimator account for this modeling uncertainty. Results of  
 the free-decay simulation are given in Figure 4  $\bar{\tau}$  for a time period of 153 s corresponding to the surge frequency. When



290 **Figure 4.** Free decay of the structure using nonlinear and linear models for a case including moorings and hydrodynamics (still water). Time  
 291 series of the main DOF.

292 hydrodynamics is included, the time responses from the linear models are in strong agreement with the nonlinear OpenFAST  
 293 results for the surge, heave, pitch, and tower fore-aft DOFs/DOF. The sway, roll, and rotor speed responses tend to drift as the  
 294 simulation time advances. The WELIB linear model has difficulty capturing the yaw response. We believe that some of the error  
 295 in the yaw signal is due to differences between the formulations of the three-dimensional rotations in OpenFAST and WELIB,  
 296 resulting in a difference of coupling between the DOFs, which we assume can be attributed to inherent differences between  
 297 linear and nonlinear models. The coefficient of determination ( $R^2$ ) is indicated in Figure 4, comparing the linear models to  
 298 the reference OpenFAST simulations for each response. In all cases, the OpenFAST linear model is closer to the nonlinear  
 299 OpenFAST model than the WELIB model. The consistency between the linear and nonlinear OpenFAST model is expected  
 because they are obtained from the same code base. The WELIB linear model had difficulty capturing the yaw response. We

300 believe that some of the error in the yaw signal is due to differences between the formulations of the three-dimensional rotations  
 301 in OpenFAST and WELIB. The difference in yaw, results in a difference of coupling between the DOF, which can explain the  
 302 differences observed in the sway, roll and rotor speed signals.

303 To further quantify the differences between the models, we compare the natural frequencies obtained using the OpenFAST  
 linear and WELIB linear models in Table 3. Overall, the frequencies between the two linear formulations agree very well (less

**Table 3.** Comparison of system frequencies obtained using the WELIB and OpenFAST linear models with and without hydrodynamics (no  
 added-added mass, damping, hydrostatics, or wave excitation)

Mode	Structure + mooring			Structure + mooring + hydrodynamics		
	OpenFAST [Hz]	WELIB [Hz]	Rel. Err [%]	OpenFAST [Hz]	WELIB [Hz]	Rel. Err [%]
Surge	0.0088	0.0088	-0.2	0.0067	0.0065	-2.4
Sway	0.0088	0.0088	-0.1	0.0067	0.0068	0.7
Yaw	0.0163	0.0162	-1.0	0.0128	0.0128	-0.3
Pitch	0.0879	0.0886	0.7	0.0253	0.0257	1.6
Roll	0.0894	0.0902	0.9	0.0256	0.0266	4.0
Heave	NA	NA	NA	0.0276	0.0276	-0.2
Tower FA	0.5782	0.5789	0.1	0.5129	0.5145	0.3

304  
 305 that than 2.5% relative error), except for the roll frequencies (4% error) with hydrodynamics. Given the results of this section,  
 306 we will continue this study using the OpenFAST linear model. We expect that continuous development of WELIB will further  
 307 narrow the gap with OpenFAST in the future.

### 308 3.4 Aerodynamic estimator

309 In Section 3.3, we indicated that the linear models were derived without accounting for aerodynamics. Instead, we choose to  
 310 include the aerodynamic contribution separately within the digital twin. The reason for this choice is that the determination of  
 311 the aerodynamic loads is essential to capturing the main loading and deflections of the structure, in particular the tower, and  
 312 the aerodynamic loads vary significantly over the range of operating conditions. Therefore, separating this contribution limits  
 313 the need to obtain different linearized models for different operating conditions. We have successfully applied this approach  
 314 in the past (Branlard et al., 2020a). In this work, we extend this approach to accommodate the floating wind application. The  
 315 different elements of the aerodynamic estimator consist of a torque estimator, aerodynamic maps, and a wind speed estimator.

#### 316 3.4.1 Kalman filter for torque estimation

317 We assume that the power and rotor speed are reliable measurement signals, and we further assume that the generator torque  
 318 (relative to the low-speed shaft) can be inferred from the power signal as:

$$319 \quad Q_g = \frac{P}{\dot{\psi}} \frac{1}{n\eta_{DT}(\dot{\psi})} \quad (2)$$

320 where  $\eta_{DT}$  is the drivetrain (gearbox and generator) efficiency, and  $n$  is the gear ratio. For the TetraSpar,  $n = 1$ , and we assume  
 321  $\eta_{DT} = 1$ . The dynamics equation of the drivetrain is modeled as:

$$322 \quad J_{DT}\ddot{\psi} = Q - Q_g \quad (3)$$

323 where  $J_{DT}$  is the inertia of the drivetrain about the shaft axis. If we assume that the generator torque is a measurement, then an  
 324 augmented Kalman filter (Lourens et al., 2012) can be used to estimate the aerodynamic torque  $Q$ , using the following state  
 325 equation:

$$326 \quad \begin{bmatrix} \dot{\psi} \\ \ddot{\psi} \\ \dot{Q} \end{bmatrix} = \begin{bmatrix} 0 & 1 & 0 \\ 0 & 0 & \frac{1}{J_{DT}} \\ 0 & 0 & 0 \end{bmatrix} \begin{bmatrix} \psi \\ \dot{\psi} \\ Q \end{bmatrix} + \begin{bmatrix} 0 \\ -\frac{1}{J_{DT}} \\ 0 \end{bmatrix} Q_g \quad (4)$$

327 A random walk approach is used for the evolution of the torque, that is,  $\dot{Q} = 0$ , and the Kalman filter adds further model noise  
 328 to this equation. The measurement equation of the Kalman filter is:

$$329 \quad \begin{bmatrix} \dot{\psi} \\ Q_g \end{bmatrix} = \begin{bmatrix} 0 & 1 & 0 \\ 0 & 0 & 0 \end{bmatrix} \begin{bmatrix} \psi \\ \dot{\psi} \\ Q \end{bmatrix} + \begin{bmatrix} 0 \\ 1 \end{bmatrix} Q_g \quad (5)$$

330 In the following, we ~~will~~ write  $\hat{Q}$ , the aerodynamic torque obtained using the method outlined above. We ~~will~~ present verifica-  
 331 tion results in Section 3.4.4.

### 332 3.4.2 Aerodynamic maps

333 It is commonly accepted that the aerodynamic ~~performances~~ performance of a wind turbine mostly depends on the tip-speed  
 334 ratio and the pitch angle of the blade. With compliant structures, the bending of the blade, the bending of the tower, and the  
 335 motions of the floating platform (in particular, the platform pitch) will also affect the aerodynamic ~~performances~~ performance.  
 336 These motions are to a large extent a function of the mean wind speed. Therefore, we ~~suggest to tabulate the aerodynamic~~  
 337 ~~performances as recommend~~ tabulating the aerodynamic performance as a function of wind speed ( $U$ ), rotor speed ( $\dot{\psi}$ ), blade  
 338 pitch ( $\theta_p$ ), and platform pitch  ~~$\phi_y$~~  ( $\phi_y$ , assumed to be in the fore-aft direction). The power and thrust coefficients, respectively  
 339 noted  $C_P$  and  $C_T$ , are precomputed using aeroelastic simulations in OpenFAST for a discrete set of values of the ~~4~~ four input  
 340 parameters. In the simulations, the blade and tower elasticity are accounted for. To limit the number of simulations, only the  
 341 points that are within reasonable proximity of the regular operating conditions of the wind turbine are computed. The 4D  
 342 aerodynamic maps are precomputed as follows:

$$343 \quad C_P(U, \dot{\psi}, \theta_p, \phi_y), \quad C_T(U, \dot{\psi}, \theta_p, \phi_y) \quad (6)$$

$$344 \quad U \in \{2, 3, \dots, 25\} \text{ m}\cdot\text{s}^{-1}, \quad \dot{\psi} \in \{5, 5.5, \dots, 18\} \text{ rpm}, \quad (7)$$

$$345 \quad \theta_p \in \{-1, 0, \dots, 30\} \text{ deg}, \quad \phi_y \in \{-10, 0, 15\} \text{ deg} \quad (8)$$

346 The precomputed values are stored in a database.

### 347 3.4.3 Wind speed estimation

348 The digital twin uses the aerodynamic map database to estimate the wind speed and aerodynamic thrust. For a given air density  
 349 ( $\rho$ ), rotor radius ( $R$ ), and ~~given measurements  $\tilde{\psi}, \tilde{\theta}_p, \tilde{\phi}_y$~~  measurements  $\tilde{\psi}, \tilde{\theta}_p, \tilde{\phi}_y$ , the aerodynamic torque and thrust are readily  
 350 obtained as a function of wind speed from the database:

$$351 \quad Q(U) = \frac{1}{2} \rho \frac{U^3}{\tilde{\psi}} \pi R^2 C_P(U, \tilde{\psi}, \tilde{\theta}_p, \tilde{\phi}_y), \quad T(U) = \frac{1}{2} \rho U^2 \pi R^2 C_T(U, \tilde{\psi}, \tilde{\theta}_p, \tilde{\phi}_y) \quad (9)$$

352 where ~~S.I.~~ SI units are assumed for all variables. For a given estimated torque ( $\hat{Q}$ ), the estimated wind speed ( $\hat{U}$ ) is found such  
 353 that:

$$354 \quad Q(\hat{U}) - \hat{Q} = 0 \quad (10)$$

355 As illustrated in Figure 5, multiple values of  $\hat{U}$  can potentially satisfy Equation 10 because the aerodynamic torque is a  
 nonlinear function of the wind speed. In such ~~cases~~ cases, we use the steady-state operating condition curve of the turbine to

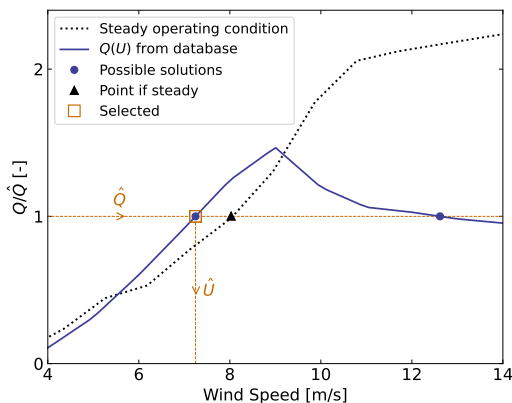


**Figure 5.** Illustration of wind speed estimation in the case where multiple wind speed values match the target torque value  $\hat{Q}$

356 ~~chese-choose~~ choose between the multiple solutions (typically two) ~~;~~ by selecting the point ~~that is~~ closest to this curve (see Figure 5).  
 358 A relaxation scheme is also used, based on the previous estimate, to alleviate sudden jumps of the estimated wind speed.

### 359 3.4.4 Verification of the aerodynamic estimator

360 To verify the aerodynamic estimator, we ran an OpenFAST simulation of the TetraSpar with the “turbulent step” wind field  
 361 mentioned in Section 2.3.2 and irregular waves computed with a significant wave height of  $H_s = 6$  m and a peak spectral  
 362 period of  $T_p = 14$ , which represent a fairly extreme sea state for the site of the TetraSpar prototype. The simulated values of  $\tilde{\psi}$ ,  
 363  $\tilde{\theta}_p$ ,  $\tilde{\phi}_y$ ,  $Q_g$  are used as direct input to the aerodynamic estimator. Comparisons of the estimates with the OpenFAST outputs are  
 364 shown in Figure 6. The shaded ~~area on the figure represent the area~~ areas on the graphs represent the areas where the generator  
 365 torque is zero (turbine spinning up) ~~;~~ and ~~;~~; therefore, the wind speed estimator is not expected to work in that region. The ~~top~~

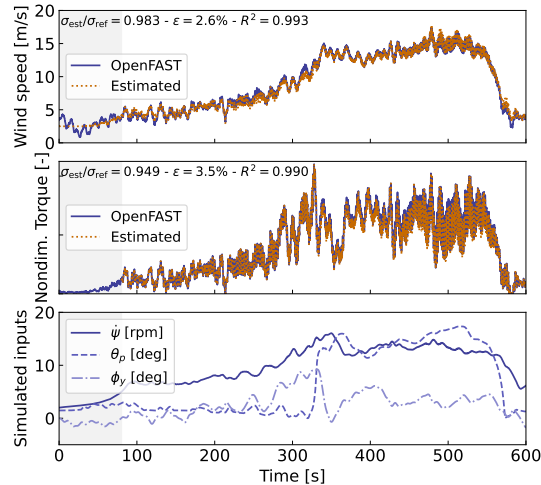


**Figure 6.** Example of aerodynamic estimation using “simulated measurements” from OpenFAST. Top: wind speed. Middle: Dimensionless torque. Bottom: structural inputs from the OpenFAST simulation provided to the estimator.

366 **tops** of the plots indicate the ratio of standard deviations, the mean relative error ( $\epsilon$ ), and the coefficient of determination ( $R^2$ ).

367 Throughout this article, we define the mean relative error of a quantity  $x$  as:

$$368 \quad \epsilon(x) = \text{mean}_i \left[ \frac{|x_{\text{est}}[i] - x_{\text{ref}}[i]|}{\text{mean}(|x_{\text{ref}}|)} \right] \quad (11)$$

369 where  $x_{\text{est}}$  is the estimated signal,  $x_{\text{ref}}$  is the reference signal, and  $x[i]$  is the value of a signal at the time step  $i$ . Using the mean  
 370 of  $|x_{\text{ref}}|$  in the denominator avoids **issue-issues** related to signals crossing 0. It results in lower mean relative error than if the  
 371 instantaneous value **was-were** used, but the metric is still indicative of how far the two signals are on average.

372 To quantify the performance of the estimator, we **reproduced-reproduce** the simulation above, but **adding-add** different noise  
 373 levels to the measurements to account for measurement errors by the sensors. A Gaussian noise signal of zero mean and  
 374 standard deviation  $r\sigma$  is added to each input, where  $r$  is the noise level and  $\sigma$  is the standard deviation of the clean input. The  
 results are shown in Table 4. As expected, the error in the estimation increases with increasing noise levels. This numerical

**Table 4.** Mean relative error ( $\epsilon$ ) of the wind speed, torque and thrust estimates for increasing noise levels.

Noise level	0%	1%	5%	10%	20%
Wind Speed	2.6%	2.6%	3.1%	4.1%	6.7%
Torque	3.5%	3.8%	5.0%	6.8%	11.1%
Thrust	4.1%	5.1%	5.6%	7.3%	11.6%

375

376 experiment provides a rough quantification of the errors that can be expected from the aerodynamic estimator.



### 377 3.5 State estimator

378 In this work, we follow a similar approach to our previous work (e.g., Branlard et al. (2020a)), (Branlard et al., 2020a), where  
 379 an augmented Kalman filter is used to estimate states and loads. The Kalman filter used in the aerodynamic estimator (Sec-  
 380 tion 3.4) is augmented with additional states and outputs. The Kalman filter uses two linear models: a state-equation, describing  
 381 the time evolution of the states, and an output equation, describing how the measurements are related to the states and inputs.  
 382 The state and output equations are written:

$$383 \quad \delta \dot{\mathbf{x}}_{\text{KF}} = \mathbf{X}_x \delta \mathbf{x}_{\text{KF}} + \mathbf{X}_u \delta \mathbf{u}_{\text{KF}} + \mathbf{w}_x \quad (12)$$

$$384 \quad \delta \mathbf{y}_{\text{KF}} = \mathbf{Y}_x \delta \mathbf{x}_{\text{KF}} + \mathbf{Y}_u \delta \mathbf{u}_{\text{KF}} + \mathbf{w}_y \quad (13)$$

385 where  $\delta \mathbf{x}_{\text{KF}}$ ,  $\delta \mathbf{u}_{\text{KF}}$ , and  $\delta \mathbf{y}_{\text{KF}}$  are the state, input, and output<sup>1</sup>, respectively;  $\mathbf{X}_x$ ,  $\mathbf{X}_u$ ,  $\mathbf{Y}_x$ , and  $\mathbf{Y}_u$  are the system matrices that  
 386 relate the different system vectors; and,  $\mathbf{w}_x$  and  $\mathbf{w}_y$  are Gaussian processes represented modeling noise. The output vector,  
 387  $\delta \mathbf{y}_{\text{KF}}$ , is also referred to as the ‘‘measurement’’ vector  $\bar{\mathbf{y}}$  because it corresponds to the measured signals. At a given time step,  
 388 the Kalman filter algorithm uses the system matrices, a set of measurements, and an **a-priori** knowledge of the model  
 389 and measurement uncertainties to estimate the state vector (Kalman, 1960; Zarchan and Musoff, 2015).

390 In this work, we design the state estimator such that the state vector contains the structural degrees of freedom ( $\delta \mathbf{q}$  and  $\delta \dot{\mathbf{q}}$ )  
 391 and the aerodynamic torque ( $Q$ ), and the input vector consists of the thrust (obtained with the aerodynamic estimator)  $\bar{\mathbf{u}}$  and  
 392 the generator torque (obtained from the power). These design choices were guided by our previous work on the topic. For  
 393 this choice of state and input variables, we build linear models for the state and output equations. We use the linear models  
 394 described in Section 3.3 (the  $\mathbf{A}$ ,  $\mathbf{B}$ ,  $\mathbf{C}$ ,  $\mathbf{D}$  matrices) to populate the system matrices of the Kalman filter. **We provide additional**  
 395 **Additional** details on how the relevant Jacobians are extracted **are given** in Section 3.6.1. Given our choice of system vectors,  
 396 the state equation is:

$$397 \quad \begin{bmatrix} \delta \dot{\mathbf{q}} \\ \delta \ddot{\mathbf{q}} \\ \dot{Q} \end{bmatrix} = \begin{bmatrix} \mathbf{0} & \mathbf{I} & \mathbf{0} \\ \mathbf{A}_{12} & \mathbf{A}_{22} & \frac{\partial \ddot{\mathbf{q}}}{\partial Q} \\ \mathbf{0} & \mathbf{0} & 0 \end{bmatrix} \begin{bmatrix} \delta \mathbf{q} \\ \delta \dot{\mathbf{q}} \\ Q \end{bmatrix} + \begin{bmatrix} \mathbf{0} & \mathbf{0} \\ \frac{\partial \ddot{\mathbf{q}}}{\partial Q_g} & \frac{\partial \ddot{\mathbf{q}}}{\partial T} \\ 0 & 0 \end{bmatrix} \begin{bmatrix} Q_g \\ T \end{bmatrix} + \mathbf{w}_x \quad (14)$$

398 where  $\bar{\mathbf{A}}_{12}$  and  $\mathbf{A}_{22}$  are the two lower blocks of the  $\mathbf{A}$  matrix, and  $\mathbf{I}$  is the identity matrix. The Jacobians with respect to the  
 399 loads are extracted from the  $\mathbf{B}$  and  $\mathbf{D}$  matrices. A random walk approach is used for the evolution of the torque  $Q$  (that is, we  
 400 set  $\dot{Q} = 0$ ). The output equation, which effectively relates the measurements to the system states and inputs, is set as:

$$401 \quad \begin{bmatrix} \delta \tilde{\mathbf{q}} \\ \dot{\psi} \\ \dot{\mathbf{r}}_N \\ Q_g \end{bmatrix} = \begin{bmatrix} \frac{\partial \tilde{\mathbf{q}}}{\partial \mathbf{q}} & \frac{\partial \tilde{\mathbf{q}}}{\partial \dot{\mathbf{q}}} & \frac{\partial \tilde{\mathbf{q}}}{\partial Q} \\ \mathbf{0} & \tilde{\mathbf{I}} & 0 \\ \frac{\partial \dot{\mathbf{r}}_N}{\partial \mathbf{q}} & \frac{\partial \dot{\mathbf{r}}_N}{\partial \dot{\mathbf{q}}} & \frac{\partial \dot{\mathbf{r}}_N}{\partial Q} \\ \mathbf{0} & \mathbf{0} & 0 \end{bmatrix} \begin{bmatrix} \delta \mathbf{q} \\ \delta \dot{\mathbf{q}} \\ Q \end{bmatrix} + \begin{bmatrix} \mathbf{0} & \mathbf{0} \\ 0 & 0 \\ \frac{\partial \dot{\mathbf{r}}_N}{\partial Q_g} & \frac{\partial \dot{\mathbf{r}}_N}{\partial T} \\ 1 & 0 \end{bmatrix} \begin{bmatrix} Q_g \\ T \end{bmatrix} + \mathbf{w}_y \quad (15)$$

<sup>1</sup>In general, the Kalman filter system vectors are different from the ones used for the linearization presented in Section 3.3, therefore the subscript  $KF$  (for Kalman Filter) is added to these vectors.

402 where  $\ddot{\mathbf{r}}_N$  is the vector of nacelle accelerations, and  $\tilde{\mathbf{q}} = \{\delta x, \delta y, \delta \phi_x, \delta \phi_y\}$  is the measurements of surge, sway, roll, and pitch  
403 as given in Table 1.

404 The state and output equations are used as part of a Kalman filter algorithm implemented in WELIB, which continuously  
405 takes as input the measurements from the wind turbine (corresponding to the left-hand side of Equation 15). The process  
406 and covariance matrices used within the Kalman filter algorithm (determining the values of  $\mathbf{w}_x$  and  $\mathbf{w}_y$ ) are populated based  
407 on the estimated standard deviations of the different states and outputs. At each time step, the thrust is estimated using the  
408 aerodynamic torque of the previous time step and used as input. The result of the Kalman filter ~~consists in~~ is the estimated  
409 states and outputs at each time step. Sample simulation results ~~will be~~ are provided in Section 4.

## 410 3.6 Virtual sensing

411 Once the states are estimated by the Kalman filter, the virtual sensing step is used to derive quantities of interest (see Figure 1).  
412 In this work, we focus on the estimation of the sectional loads along the tower using a physics-based model. We investigate  
413 two methods to obtain these loads.

### 414 3.6.1 OpenFAST linearization outputs

415 The first method consists of using the linearization outputs of OpenFAST, namely, using a subset of the equation  $\delta \mathbf{y} = \mathbf{C} \delta \mathbf{x} +$   
416  $\mathbf{D} \delta \mathbf{u}$  (see Section 3.3.1). In general, if a ~~QoI~~ quantity of interest is present in the output vector of OpenFAST, it can be retrieved  
417 as follows. If the variable is located at the row index  $k$  in the vector  $\mathbf{y}$ , then this variable can be obtained from the states and  
418 inputs as:

$$419 \quad [\mathbf{y}]_k = [\delta \mathbf{y}]_k + [\mathbf{y}_0]_k = [\mathbf{C}]_k \delta \mathbf{x} + [\mathbf{D}]_k \delta \mathbf{u} + [\mathbf{y}_0]_k \quad (16)$$

420 where  $[\cdot]_k$  indicates that the row  $k$  of the matrix or column vector is used. In our case,  $[\mathbf{y}]_k$  in Equation 16 would ~~for instance~~  
421 be the sectional fore-aft bending moment at the height  $z_j$  along the tower, noted  $\mathcal{M}_y(z_j)$ . The advantages of using this method  
422 are multiple: 1) the method is directly applicable to any other outputs computed by OpenFAST, 2) the calculation procedure  
423 is linear and therefore computationally efficient, 3) if strain measurements are available at given heights, the rows  $[\mathbf{C}]_k$  and  
424  $[\mathbf{D}]_k$  could be included in the output equation of the Kalman filter (Equation 15) to provide information about the model's  
425 expectation of these measurements, ~~and~~ 4) the underlying linear model is consistent with the nonlinear model of OpenFAST.  
426 The downside of the method is its linearity, in the sense that it is only valid close to the operating point and could lack important  
427 nonlinear effects. The values of  $[\mathbf{C}]_k$ ,  $[\mathbf{D}]_k$ , and  $[\mathbf{y}_0]_k$  would potentially need to be reevaluated if the system operates away  
428 from the linearized operating point. One possible solution ~~would be~~ is to introduce gain-scheduling to ~~continuously~~ modify the  
429 linear system based on the estimated wind speed. ~~In this work, we used one operating point only and obtained results with fair~~  
430 ~~accuracy (see Section 4). We nevertheless expect that to better represent the different operating regions of a pitch-regulated~~  
431 ~~wind turbine, three to five linear models, stitched together through gain-scheduling would be needed.~~

### 432 3.6.2 Nonlinear calculation (WELIB)

433 An alternative method consists of computing the section loads based on first principles using the formulation presented in  
434 Branlard (2019). The calculation requires a knowledge of the tower-top loads and the full kinematics of the tower and nacelle  
435 (position, velocity, and acceleration). At a given time step, the kinematics are computed based on  $\mathbf{q}$ ,  $\dot{\mathbf{q}}$ , and  $\ddot{\mathbf{q}}$ . The tower-  
436 top loads are estimated based on the aerodynamic loads and the inertial loads of the rotor-nacelle assembly. We describe  
437 the method in more ~~details-detail~~ in Appendix D. The advantages are that nonlinearities are accounted for and the model is  
438 valid ~~irrespectively-irrespective~~ of the operating condition. The downside is that this method does not provide any of the four  
439 advantages offered by the OpenFAST linearization method.

### 440 3.6.3 Verification of the section loads calculation

441 To verify the calculation of the section loads, we use the same “turbulent step” wind field and irregular sea state that ~~was~~  
442 ~~were~~ used in Section 3.4.4. We assume that the time series of  $\mathbf{q}$ ,  $\dot{\mathbf{q}}$  and  $\ddot{\mathbf{q}}$  are entirely known, extracted from the OpenFAST  
443 simulation. These time series are provided to the two section loads algorithms: the WELIB nonlinear algorithm ~~;~~ and the  
444 OpenFAST linear algorithm.

445 We run two sets of virtual sensing. In the “ideal” set, the loads at the tower top are extracted from OpenFAST results and  
446 provided to the two virtual sensing algorithms. In this ideal case, the linearized operating points of the OpenFAST linear model  
447 is set as the mean of each of the OpenFAST time series values. Results for the ideal case are ~~provided-illustrated~~ in Figure 7.  
The two algorithms are able to reproduce the section loads of OpenFAST with relatively high accuracy, which verifies our two

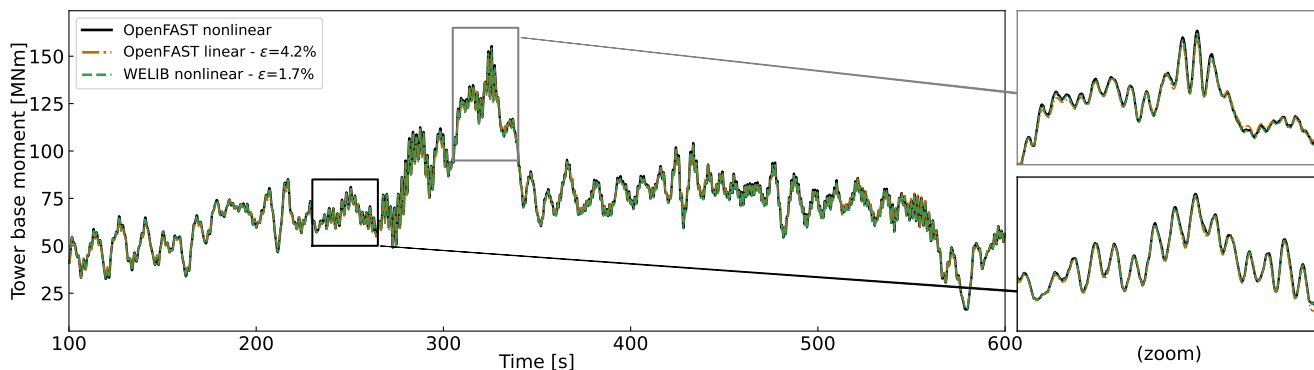


**Figure 7.** Tower fore-aft bending moment for the “turbulent step” and an irregular sea state as calculated by OpenFAST and compared to the WELIB nonlinear and OpenFAST linear method. The motion of the structure is determined by OpenFAST and provided to the two algorithms. The tower-top loads are also provided to the algorithms (“ideal” case, as opposed to Figure 8).

448

449 calculation procedures.

450 In the second set, labeled “unknown thrust~~;~~,” the tower top loads are not provided to the algorithms~~;~~~~but;~~ instead, the  
451 aerodynamic estimator mentioned in Section 3.4.4 is used to estimate the aerodynamic loads. This time, we do not set the

452 linearized operating point of the OpenFAST linear model to the mean value of the time series, ~~but~~; we set it to the static  
453 equilibrium (without loading).

The results are ~~provided~~ ~~illustrated~~ in Figure 8. The accuracy of the section loads calculation is seen to deteriorate when the

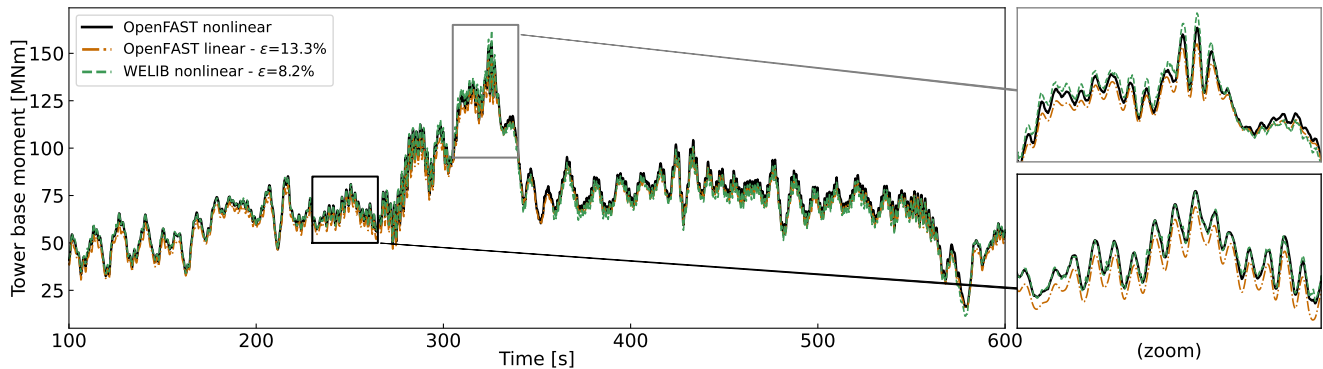


**Figure 8.** Tower fore-aft bending moment for the “turbulent step” and an irregular sea state as calculated by OpenFAST and compared to the WELIB nonlinear and the OpenFAST linear method. The motion of the structure is determined by OpenFAST and provided to the two other algorithms. The tower-top loads are estimated using the aerodynamic estimator (“unknown thrust” case, as opposed to the ideal case presented in Figure 7).

454  
455 aerodynamic loads are estimated with the aerodynamic estimator, which is expected. The damage equivalent load computed  
456 with a Wöhler slope of  $m = 5$  is found to be 3.7% lower with the OpenFAST linear method and 1.2% lower with the YAMS  
457 nonlinear method compared to the value for reference signal.

458 The ~~performances~~ ~~performance~~ of both algorithms ~~remain satisfactory because we observe that~~ ~~remains~~ ~~satisfactory~~ ~~because~~  
459 the extrapolated signals follow the reference OpenFAST nonlinear simulation. The relative error obtained with the OpenFAST  
460 linear algorithm is higher (13.3%) than the one obtained using the WELIB nonlinear method (8.2%). The main source of error  
461 in the linear model is associated with the fact that the linearization point was not tuned for this specific simulation. It is our  
462 simplifying design choice to use only one linearization operating point throughout. Because of the loss of accuracy associated  
463 with this design choice, we ~~will~~ use the WELIB nonlinear algorithm in the digital twin for the calculation of section loads.

464 ~~We note that the variable that affects the most~~ After performing a sensitivity analysis on the inputs and states of the system,  
465 we observed that the variables that most affect the fore-aft section loads ~~is~~ ~~are~~ the platform pitch ( $\phi_y$ ), the tower fore-aft  
466 bending degree of freedom ( $q_t$ ), and ~~then~~, the aerodynamic thrust. In this section, we assumed that all the states were known  
467 (including  $\phi_y$  and  $q_t$ ), leading to great accuracy in the estimation of the section loads. The final verification step ~~consists of~~  
468 ~~involves~~ providing estimated states to the algorithm, which is the topic of the next section.

## 469 4 Applications of the digital twin

470 In Section 3, we discussed how the different components of the digital twin were introduced and tested using increasing level  
471 of complexity. In this section, we combine-discuss combining the different components to form the digital twin. We begin  
472 using numerical experiments from OpenFAST (see Section 2.3.2), similar to what was done in-the-previous-section previously,  
473 before using measurements from the TetraSpar prototype.

### 474 4.1 Numerical experiment

475 First, we use the same “turbulent step” wind field and sea state that was used throughout Section 3. The augmented states of the  
476 system are determined at each time step using the state estimator described in Section 3.5. The measurements (see Table 1) are  
477 taken from the nonlinear OpenFAST simulation. The wind speed and aerodynamic loads are estimated using the aerodynamic  
478 estimator described in Section 3.4. The linear model is derived from linearized OpenFAST while-, and the section loads in the  
479 tower are obtained using the WELIB virtual sensing algorithm described in Section 3.6. The estimates from the digital twin are  
compared with the reference nonlinear OpenFAST simulation results in Figure 9. A visual inspection of the time series reveals

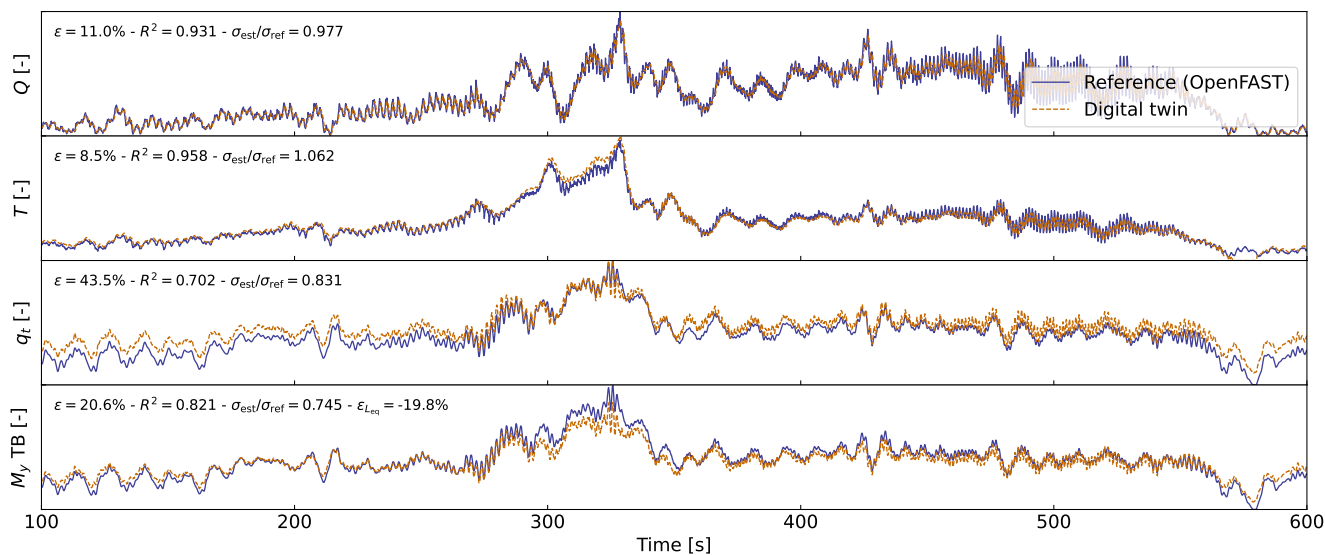


**Figure 9.** Estimated signals from the digital twin compared to results from an a nonlinear OpenFAST simulation using the turbulent-step numerical experiment. From top to bottom: aerodynamic torque ( $Q$ ), aerodynamic thrust ( $T$ ), tower-top position ( $q_t$ ), tower-bottom fore-aft bending moment ( $M_y$ , TB). Results are made dimensionless for confidentiality reasons.

480

481 that the digital twin is able to capture the main trends and fluctuations of the different signals. The match can be considered  
482 remarkable given that only the sensors provided in Table 1 are used by the digital twin. Metrics such as mean relative error ( $\epsilon$ )  
483 and coefficient of determination ( $R^2$ ) are indicated on the figure. Despite the visually appealing match, the metrics indicate  
484 that the tower-bottom moment has a mean error of  $\epsilon = 21\%$ . The damage equivalent load of the tower-bottom moment is

485 underestimated by  $\tilde{\epsilon}_{L_{eq}} = -21\%$ , where we define:

$$486 \quad \tilde{\epsilon}(L_{eq}) = \frac{L_{eq,est} - L_{eq,ref}}{L_{eq,ref}} \quad (17)$$

487 Differences in damage equivalent loads typically indicate differences in the frequency content of the signals. We compare the frequency content of the estimated signals with the reference signals in Figure 10. The low-frequency content (below 1 Hz) is

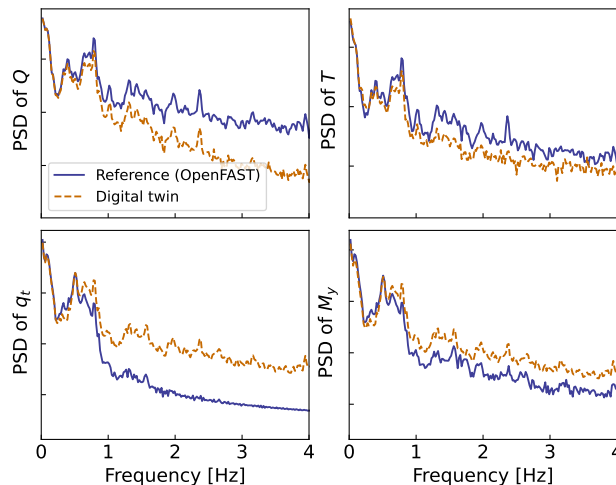


**Figure 10.** Power spectral density (PSD) of the time series presented in Figure 9. A logarithmic scale is used on the  $y$  axis.

488 captured well, in line with the visual inspection of Figure 9. Unfortunately, no clear trend is found for the **high-frequency-high-**  
 489 **frequency** content: the power spectra of the aerodynamic loads indicate an underestimation, whereas the spectra of the tower-top  
 490 position and tower-bottom bending moment tend to have higher energy content. As shown in previous studies (Branlard et al.,  
 491 2020a), **adequate**-filtering of the input measurements can be used to tune the energy content at high frequencies. **The method**  
 492 **is yet unsatisfactory** because it acts as an artificial rebalancing of energy content to achieve the desired DEL value. **Both low**  
 493 **and high frequency content contribute to the DEL values, therefore, we believe that systematic improvement is only possible**  
 494 **through modeling improvements and higher observability of the states by the Kalman filter.**

496 To quantify the errors in the estimation under a wider set of operating conditions, we **ran-run** 10-min simulations for a  
 497 set of wind speeds under normal turbulent conditions and sea states. We **selected-select** wind speeds from 5 to 20 m/s using  
 498 10 different seeds per bin of wind speed. The seeds are used to **randomise-randomize** the turbulent field and sea states. The  
 499 wind speed range is selected **such-so** as to avoid cut-in and cut-out events where the aerodynamic estimator is not expected  
 500 to perform well. The turbulence intensity is selected based on the normal turbulence model for a turbine of class “A<sup>2</sup>.” The  
 501 wave height and wave period are set as a function of the wind speed as:  $H_s(U) = 0.16U + 1$  and  $T_p = 0.09U + 5.57$ , **based**  
 502  $T_p(U) = 0.09U + 5.57$ . **The  $H_s$  and  $T_p$  relationships were obtained by performing a linear regression on the sea state and wind**  
 503 **measurements at the test site. OpenFAST simulations were-are** run for each case, and then the digital twin **was-is** run using  
 504 these numerical measurements. A summary of the mean relative error on some key estimated quantities is given in Figure 11.

We observe that the mean relative error of the wind speed and aerodynamic loads are is between 5% and 15% with a tendency

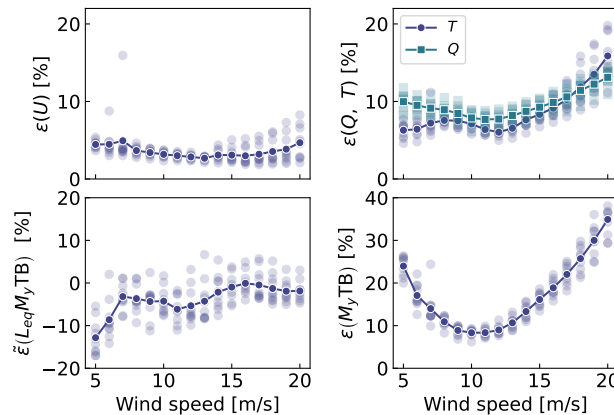


**Figure 11.** Mean relative error of estimated signals for various wind speed and seeds. Clockwise from top left: wind speed ( $U$ ), aerodynamic loads, tower-bottom moment ( $M_y$  TB), and damage equivalent load of the tower-bottom moment ( $L_{eq}, M_y$  TB). The individual simulations are indicated by transparent markers. The average over each seed is indicated using plain solid lines.

505

506 for larger errors on the aerodynamic loads at low and high wind speeds. The error further propagates within the system, and the  
 507 tower-bottom moment is estimated with a relative error between 10% and 40%. The error levels indicate that the aerodynamic  
 508 estimator, which is based on quasi-steady rotor-averaged aerodynamics, cannot fully capture the dynamic aerodynamic state  
 509 of the rotor in floating conditions. In general, the digital twin lacks sufficient information to fully capture the tower-top loads  
 510 and the frequency content of the system. It is expected that placing the placement of additional sensors, such as accelerometers  
 511 or load cells, along the tower, can significantly improve the estimation of the tower loads (in that case, we would either use  
 512 OpenFAST linearization outputs, or, or an extended Kalman filter and a nonlinear model for the outputs). As seen in Figure 11,  
 513 the relative error levels on the damage equivalent loads are between  $-10\%$  and  $5\%$ , with the loads being either overestimated  
 514 or underestimated depending on the wind speed. The structural health monitoring system could potentially use the estimated  
 515 error levels indicated in Figure 11 to provide a confidence interval on the fatigue lifetime of the tower. We note that these  
 516 error levels represent a best-case scenario, best-case scenario because we assumed that no noise or biases were present in the  
 517 measurements. We expect the error levels to increase with additional measurement noise.

## 518 4.2 Estimations using measurements from the full-scale prototype

519 In this section, we use measurements from the full-scale TetraSpar prototype installed off the Norwegian coast. Four days of  
 520 data were selected based on data availability; a wide range of wind speeds are present in the time series (ranging from 4 to 24.5  
 521 m/s with an overall mean of 8.9 m/s). Two days were selected in summer and two in winter to account for potential seasonality.  
 522 Apart from these criteria, the selection of time series can be considered random. The measurement data is are stored as 10-min  
 523 time series sampled at 25 Hz. The total number of 10-min samples used over the four days is 576. The measurement data is

524 are provided to the digital twin to perform the state estimation and virtual sensing. ~~The~~The prototype is equipped with load  
 525 cells at the tower top, middle, and bottom and nacelle wind speed measurements. We use these measurements to compare with  
 526 the digital twin estimates.

527 We begin by highlighting the computational time of the current procedure, as computational efficiency is crucial to achieve  
 528 our digital twin vision. The state estimation is currently 10 times faster than ~~realtime~~real time. The virtual sensing step is ~~half~~  
 529 ~~realtime~~twice as fast as real time, but computational improvements are possible, in particular, by using a compiled language  
 530 instead of Python. ~~The prototype is equipped with load cells at the tower top, middle and bottom, and nacelle wind speed~~  
 531 ~~measurements. We use these measurements to compare with~~For reference, OpenFAST simulations of the full TetraSpar model  
 532 (with substructure flexibility) typically run 3 times slower than real time, and a reduced-order OpenFAST model with 8 DOF  
 533 runs 1.1 times slower. Currently, real time estimation cannot be achieved with OpenFAST. Reduced-order modeling techniques,  
 534 such as the ones presented in this article, are necessary to implement an online digital twin. Yet, if the digital twin ~~estimates~~is  
 535 run as a postprocessing step, then parallelization using multiple CPUs could be used, e.g., processing different time periods of  
 536 the day.

537 A sample of results is provided in Figure 12. The figure illustrates a selected case where the estimation of the tower load  
 is reasonably accurate, with an error on the damage equivalent load of only 0.4%. We note that the wind speed from the

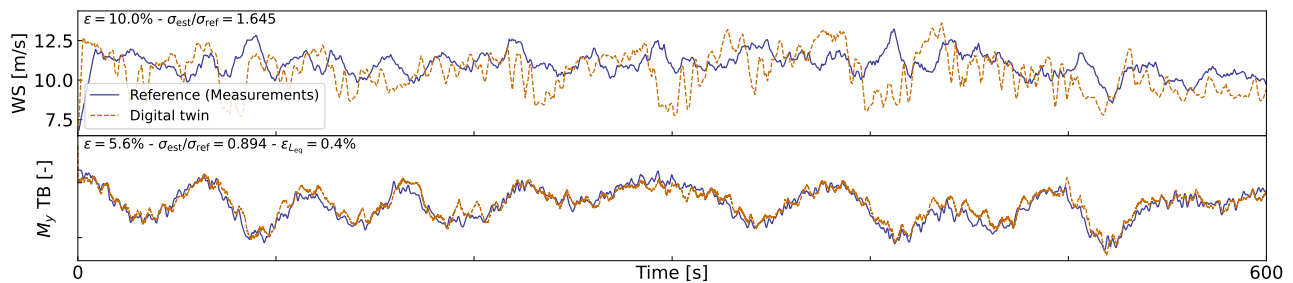


**Figure 12.** Comparison of digital twin outputs with wind speed and tower-bottom moment measurements from the TetraSpar prototype. The measured wind speed comes from a nacelle anemometer and therefore is expected to differ from the rotor-averaged value estimated by the digital twin.

538  
 539 measurement is a point measurement ~~ȳ~~(nacelle anemometer, in the wake of the turbine), and it is therefore not expected to be  
 540 in strong agreement with the digital twin estimate, which is representative of a rotor-averaged wind speed.

541 An aggregate of results from all the 10-min digital twin runs is illustrated in Figure 13. The figure shows relative errors in  
 542 wind speed, thrust, and damage equivalent loads at the tower bottom and tower middle. As indicated previously, the wind speed  
 543 from the digital twin and the measurements are different quantities, but the level of error obtained indicates that the digital twin  
 544 is able to capture the main level of wind speed. The aerodynamic thrust from the aerodynamic estimator is compared with  
 545 the load cell at the tower top in the fore-aft direction. This is a crude first-order approximation ~~ȳ~~(e.g., neglecting inertial and  
 546 ~~gravitational loads, nacelle tilting and shaft bending~~), but the overall estimated levels appears to be ~~on-average~~, on average,  
 547 around 10% from the measured ones. The tower damage equivalent loads are ~~on-average~~, on average, within  $\pm 10\%$  of the



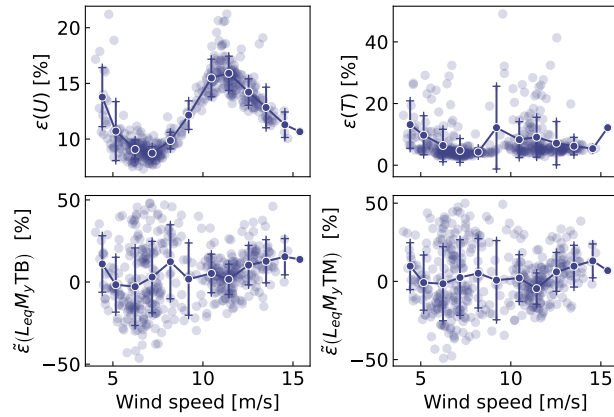


**Figure 13.** Similar to Figure 11 but using measurements from the Tetra Spar prototype. Each marker indicates a 10-min simulation result. Solid lines are bin averages. The whiskers indicate the standard deviation in each bin. The bottom plots are for the tower bottom (TB) and tower middle (TM) bending moments.

548 values obtained from the measurements, but some cases show errors ranging between  $\pm 50\%$ . To give perspective on the large error values taken by the metrics, we illustrate two cases with large errors in Figure 14 and Figure 15. In both cases, we observe

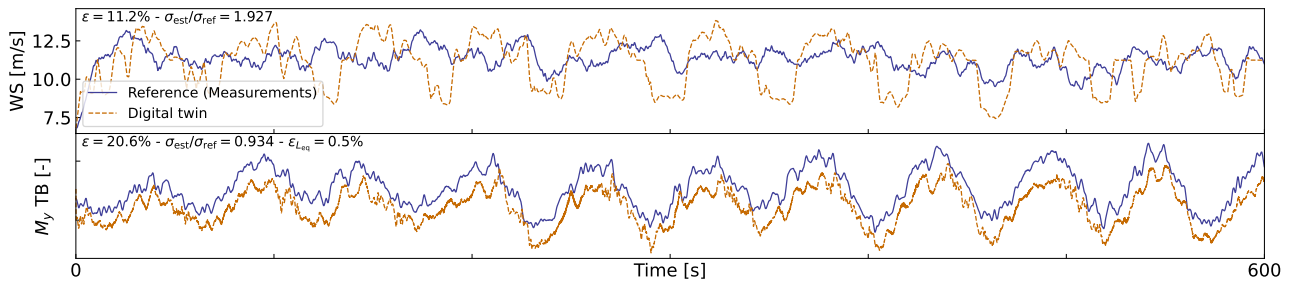


**Figure 14.** Similar to Figure 12, but for a case where a clear offset is present in the tower loads.

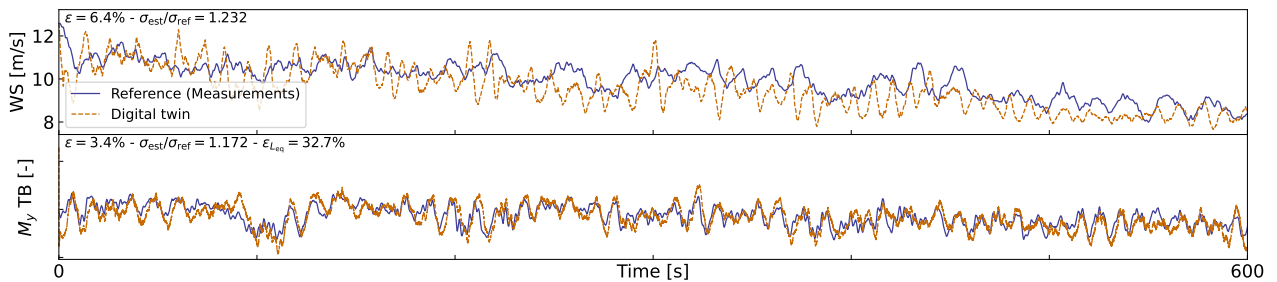


**Figure 15.** Similar to Figure 12, but for a case where a large error in damage equivalent load is observed.

549

550 that the estimator is capturing the trends and low frequencies with ~~accuracies~~ accuracy that, from a pure qualitative perspective,  
551 would appear satisfactory. As seen in Figure 14, an offset is present in the signal, which indicates that some physics might be  
552 missing from the load virtual sensing, or that the state estimator is failing. ~~Measurement errors could also affect the results, but~~  
553 ~~no systematic error was detected over the time period investigated. It is therefore difficult to conclude as to what is the main~~  
554 ~~source of error.~~ In Figure 14, the overall load level is captured well, but the error in the damage equivalent load is  $\epsilon_{Leq}$  is 33%.  
555 As illustrated in Figure 10, our current method fails at capturing the high-frequency content of the signals, which can have a  
556 significant impact on the accuracy of the damage equivalent loads. ~~In spite of~~ Despite these challenges, the average accuracy  
557 of 10% is promising and indicates that the current methodology can be used to reconstruct some structural and environmental  
558 signals from a limited number of ~~readily-available~~ readily available sensors.

## 559 5 Conclusions

560 In this work, we implemented, verified, and validated a physics-based digital twin solution applied to a floating offshore wind  
561 turbine. The work focused on the estimation of the aerodynamic loads and the section loads along the tower, using a set of  
562 measurements that we expect to be available on any existing wind turbine (power, pitch, rotor speed, and tower acceleration)  
563 ~~;~~ and motion sensors that are likely to be standard measurements for a floating platform (inclination and GPS sensors). The  
564 key concept behind our approach ~~consists of using:~~ uses 1) a Kalman filter to estimate the structural states based on a linear  
565 model of the structure and measurements from the turbine, 2) an aerodynamic estimator, and 3) a physics-based virtual sensing  
566 procedure to obtain the loads along the tower. An important part of the work ~~consisted of~~ was developing the methodology  
567 and implementing the tools and models necessary for the aerodynamic estimation, state estimation, and load virtual sensing.  
568 We explored two different pathways to obtain models: a suite of Python tools ~~;~~ ~~or~~ and OpenFAST linearization. We used  
569 components from both approaches for the digital twin.

570 Using numerical experiments, we found that the accuracy of the individual models ~~were typically in~~ was typically on the  
571 order of 5%. When comparing the digital twin estimations with the measurements from the TetraSpar prototype, the errors  
572 increased to 10%–15% on average for the quantities of interest. Overall, the accuracy of the results appeared promising given  
573 the scope of our work, which aimed ~~at illustrating to illustrate~~ a proof of concept for a floating wind turbine digital twin. We  
574 observed ~~a~~ non-negligible scatter of results for the estimation of the tower damage equivalent loads that we attributed to the  
575 difficulty of capturing high-frequency content.

576 Future work ~~;~~ should therefore explore possible improvements of the method to address this issue.

577 Additional improvements could include: 1) gain-scheduling of the linear models ~~;~~ ~~to extend the domain of validity of the~~  
578 ~~linear models used and reduce the modeling error,~~ 2) using nonlinear models and extended Kalman filtering techniques ~~;~~ ~~to lift~~  
579 ~~the linear assumptions that challenges the aerodynamics, hydrodynamics and structural dynamics,~~ 3) introducing additional  
580 degrees of freedom and a full account of the yawing of the nacelle ~~;~~ ~~to increase the fidelity of the models and account for the~~  
581 ~~flexibility of the floater,~~ 4) adding a model to account for wave excitation forces ~~;~~ ~~to account for hydrodynamic loads and likely~~  
582 ~~improve the estimation of member-level loads,~~ 5) introducing additional measurements ~~;~~ ~~to improve the state estimation and~~

583 increase the observability of the state, 6) improving the robustness of the aerodynamic estimator (~~in particular~~in particular,  
584 beyond the cut-in and cut-out wind speed), and speeds, to apply the digital twin when the turbine is not operating, and, 7)  
585 expanding the virtual sensing steps to estimate additional signals.

586 *Author contributions.* EB implemented the digital twin and wrote the main corpus of this paper. JJ, CB and JZ provided continuous feedback  
587 on the project and reviewed the article.

588 *Competing interests.* No competing interests are present.

589 *Code availability.* The source code of the digital twin and examples using a generic spar turbine are provided in the GitHub repository (Bran-  
590 lard, 2023a).

591 *Acknowledgements.* This work was authored in part by the National Renewable Energy Laboratory, operated by Alliance for Sustainable  
592 Energy, LLC, for the U.S. Department of Energy (DOE) under Contract No. DE-AC36-08GO28308. Funding provided by U.S. Department  
593 of Energy Office of Energy Efficiency and Renewable Energy Wind Energy Technologies Office. The views expressed in the article do  
594 not necessarily represent the views of the DOE or the U.S. Government. The U.S. Government retains and the publisher, by accepting the  
595 article for publication, acknowledges that the U.S. Government retains a nonexclusive, paid-up, irrevocable, worldwide license to publish or  
596 reproduce the published form of this work, or allow others to do so, for U.S. Government purposes.

597 *Financial support.* This work was funded under the Technology Commercialization Fund Project, supported by DOE’s Wind Energy Tech-  
598 nologies Office.

## 599 **Appendix A: Linearization of the equations of motion with augmented inputs**

600 In this section, we describe the procedure used to linearize the structural equations of motion without a knowledge of the external loads,  
601 which is used to obtain Equation 1. We write the implicit form of the equations of motion as

$$602 \mathbf{e}(\mathbf{q}, \dot{\mathbf{q}}, \ddot{\mathbf{q}}, \tilde{\mathbf{u}}, t) = \mathbf{0} \tag{A1}$$

603 where  $\mathbf{q}$ ,  $\dot{\mathbf{q}}$ ,  $\ddot{\mathbf{q}}$  and  $\tilde{\mathbf{u}}$  are the degrees of freedom, velocities, accelerations, and “augmented inputs” of the model, respectively. The term  
604 augmented input is used because the external loads are included in this vector. The external loads are (in general) a function of the degrees  
605 of freedom. Therefore, we write the augmented input vector as:

$$606 \tilde{\mathbf{u}} = \tilde{\mathbf{u}}(\mathbf{q}, \dot{\mathbf{q}}, \ddot{\mathbf{q}}, \mathbf{u}) \tag{A2}$$

607 where  $\mathbf{u}$  is the vector of inputs in the classical sense, that is, consisting of system inputs that do not depend on the degrees of freedom (for  
608 instance, the wave elevation). The operating point is written using the subscript “0”, and is defined as:

$$609 \quad \mathbf{e}(\mathbf{q}_0, \dot{\mathbf{q}}_0, \ddot{\mathbf{q}}_0, \tilde{\mathbf{u}}_0, t) = \mathbf{0} \quad (\text{A3})$$

610 We perturb each variable, as  $\mathbf{q} = \mathbf{q}_0 + \delta\mathbf{q}$ ,  $\dot{\mathbf{q}} = \dot{\mathbf{q}}_0 + \delta\dot{\mathbf{q}}$ , etc., where  $\delta$  indicates a small perturbation of the quantities. The perturbation of the  
611 augmented input is then:

$$612 \quad \tilde{\mathbf{u}} = \tilde{\mathbf{u}}(\mathbf{q}_0, \dot{\mathbf{q}}_0, \ddot{\mathbf{q}}_0, \mathbf{u}_0) + \left. \frac{\partial \tilde{\mathbf{u}}}{\partial \mathbf{q}} \right|_0 \delta\mathbf{q} + \left. \frac{\partial \tilde{\mathbf{u}}}{\partial \dot{\mathbf{q}}} \right|_0 \delta\dot{\mathbf{q}} + \left. \frac{\partial \tilde{\mathbf{u}}}{\partial \ddot{\mathbf{q}}} \right|_0 \delta\ddot{\mathbf{q}} + \left. \frac{\partial \tilde{\mathbf{u}}}{\partial \mathbf{u}} \right|_0 \delta\mathbf{u} \quad (\text{A4})$$

613 where  $|_0$  indicates that the expressions are evaluated at the operating point. The linearized equations are obtained using a [Taylor-Series](#)  
614 [Taylor-series](#) expansion:

$$615 \quad \left[ M_0 - Q_0 \left. \frac{\partial \tilde{\mathbf{u}}}{\partial \ddot{\mathbf{q}}} \right|_0 \right] \delta\ddot{\mathbf{q}} + \left[ C_0 - Q_0 \left. \frac{\partial \tilde{\mathbf{u}}}{\partial \dot{\mathbf{q}}} \right|_0 \right] \delta\dot{\mathbf{q}} + \left[ K_0 - Q_0 \left. \frac{\partial \tilde{\mathbf{u}}}{\partial \mathbf{q}} \right|_0 \right] \delta\mathbf{q} = Q_0 \left. \frac{\partial \tilde{\mathbf{u}}}{\partial \mathbf{u}} \right|_0 \delta\mathbf{u} \quad (\text{A5})$$

616 with

$$617 \quad M_0 = - \left. \frac{\partial \mathbf{e}}{\partial \ddot{\mathbf{q}}} \right|_0, \quad C_0 = - \left. \frac{\partial \mathbf{e}}{\partial \dot{\mathbf{q}}} \right|_0, \quad K_0 = - \left. \frac{\partial \mathbf{e}}{\partial \mathbf{q}} \right|_0, \quad Q_0 = \left. \frac{\partial \mathbf{e}}{\partial \mathbf{u}} \right|_0 \quad (\text{A6})$$

618 and where  $M_0$ ,  $C_0$ ,  $K_0$  are the linear mass, damping, and stiffness matrices, and  $Q_0$  is the linear forcing vector, also called the input matrix.

## 619 Appendix B: Transfer of a Jacobian from one destination point to another

620 The Jacobians provided by OpenFAST and MAP are provided at given nodes of the structure (e.g., the hydrodynamic nodes, or the fairleads).  
621 In this section, we highlight the procedure to transfer these Jacobians to another node (the platform reference point) assuming a rigid-body  
622 relationship between the nodes. The procedure is used in this work to compute the linear  $6 \times 6$  matrix for the hydrodynamics and mooring  
623 dynamics in Section 3.3.2. We obtain different relationships depending [if-on whether](#) the destination point is assumed to be displaced or not  
624 [-\(see different subsections below\)](#).

### 625 B1 Transfer of Jacobians between two points

We consider a point source (noted  $S$ ) and a destination point (noted  $D$ ). The notations are illustrated in Figure B1. We assume [a-rigid-body](#)

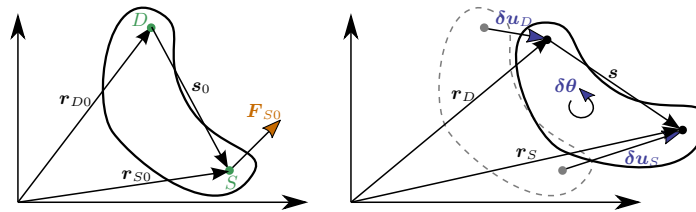


**Figure B1.** Rigid-body kinematics with the loads from one source point ( $S$ ) transferred to a destination point ( $D$ ), assuming small motion of the points.

626

627 ~~relationship between~~ that the two points ~~belong to a rigid body~~. The forces and moments at the destination and source are related as follows:

$$628 \quad \mathbf{F}_D = \mathbf{F}_S \quad (\text{B1})$$

$$629 \quad \mathbf{M}_D = \mathbf{M}_S + \tilde{\mathbf{s}} \mathbf{F}_S \quad (\text{B2})$$

630 where  $\mathbf{s} = \mathbf{r}_S - \mathbf{r}_D$  is the vector from destination point to the source point,  $\mathbf{F}_S$  and  $\mathbf{M}_S$  are the force and moments, respectively, at point  
631  $S$ , and the tilde notation refers to the skew symmetric matrix, which is a matrix representation of the cross product. We seek to linearize  
632 Equation B1 and Equation B2 for small displacements and rotations of the destination and source nodes. In particular, we seek to express  
633 the Jacobians at the destination node as a function of the source node, assuming a rigid-body relationship between the two. The rigid-body  
634 relationship linking the small displacements ( $\delta \mathbf{u}$ ) and small rotations ( $\delta \boldsymbol{\theta}$ ) of the source and destination points is:

$$635 \quad \delta \mathbf{u}_D = \delta \mathbf{u}_S + \tilde{\mathbf{s}}_0 \delta \boldsymbol{\theta}_S$$

$$636 \quad \delta \boldsymbol{\theta}_D = \delta \boldsymbol{\theta}_S \quad (\text{B3})$$

637 where  $\mathbf{s}_0$  is the vector between the source and destination points at the operating point (prior to the perturbation). The Jacobians of the  
638 transformations given in Equation B3(, and its inverse), are:

$$639 \quad \begin{bmatrix} \frac{\partial \mathbf{u}_D}{\partial \mathbf{u}_S} & \frac{\partial \mathbf{u}_D}{\partial \boldsymbol{\theta}_S} \\ \frac{\partial \boldsymbol{\theta}_D}{\partial \mathbf{u}_S} & \frac{\partial \boldsymbol{\theta}_D}{\partial \boldsymbol{\theta}_S} \end{bmatrix} = \begin{bmatrix} \mathbf{I} & \tilde{\mathbf{s}}_0 \\ \mathbf{0} & \mathbf{I} \end{bmatrix}, \quad \begin{bmatrix} \frac{\partial \mathbf{u}_S}{\partial \mathbf{u}_D} & \frac{\partial \mathbf{u}_S}{\partial \boldsymbol{\theta}_D} \\ \frac{\partial \boldsymbol{\theta}_S}{\partial \mathbf{u}_D} & \frac{\partial \boldsymbol{\theta}_S}{\partial \boldsymbol{\theta}_D} \end{bmatrix} = \begin{bmatrix} \mathbf{I} & -\tilde{\mathbf{s}}_0 \\ \mathbf{0} & \mathbf{I} \end{bmatrix} \quad (\text{B4})$$

640 To linearize Equation B1 and Equation B2, we introduce the following perturbations:

$$641 \quad \mathbf{F}_D = \mathbf{F}_{D0} + \delta \mathbf{F}_D, \quad \mathbf{F}_S = \mathbf{F}_{S0} + \delta \mathbf{F}_S \quad (\text{B5})$$

$$642 \quad \mathbf{M}_D = \mathbf{M}_{D0} + \delta \mathbf{M}_D, \quad \mathbf{M}_S = \mathbf{M}_{S0} + \delta \mathbf{M}_S, \quad (\text{B6})$$

643 where the subscript 0 indicates values at the operating point. At the operating point, Equation B1 and Equation B2 are satisfied, that is:

$$644 \quad \mathbf{F}_{D0} = \mathbf{F}_{S0} \quad (\text{B7})$$

$$645 \quad \mathbf{M}_{D0} = \mathbf{M}_{S0} + \tilde{\mathbf{s}}_0 \mathbf{F}_{S0} \quad (\text{B8})$$

## 646 **Transfer of forces**

647 Inserting Equation B5 into Equation B1 leads to:

$$648 \quad \mathbf{F}_{D0} + \delta \mathbf{F}_D = \mathbf{F}_{S0} + \delta \mathbf{F}_S \quad (\text{B9})$$

649 ~~Which~~which, using Equation B7, leads to:

$$650 \quad \delta \mathbf{F}_D = \delta \mathbf{F}_S \quad (\text{B10})$$

651 The Jacobians of the loads at node  $D$  with respect to the displacements at node  $D$  are then obtained by applying the chain rule to Equation B10  
652 and making use of the Jacobian of the displacements given on the right of Equation B4. For instance, for the force:

$$653 \quad \frac{\partial \mathbf{F}_D}{\partial \mathbf{u}_D} = \frac{\partial \mathbf{F}_S}{\partial \mathbf{u}_S} \frac{\partial \mathbf{u}_S}{\partial \mathbf{u}_D} + \frac{\partial \mathbf{F}_S}{\partial \boldsymbol{\theta}_S} \frac{\partial \boldsymbol{\theta}_S}{\partial \mathbf{u}_D} = \frac{\partial \mathbf{F}_S}{\partial \mathbf{u}_S}$$

$$654 \quad \frac{\partial \mathbf{F}_D}{\partial \boldsymbol{\theta}_D} = \frac{\partial \mathbf{F}_S}{\partial \mathbf{u}_S} \frac{\partial \mathbf{u}_S}{\partial \boldsymbol{\theta}_D} + \frac{\partial \mathbf{F}_S}{\partial \boldsymbol{\theta}_S} \frac{\partial \boldsymbol{\theta}_S}{\partial \boldsymbol{\theta}_D} = \frac{\partial \mathbf{F}_S}{\partial \boldsymbol{\theta}_S} - \frac{\partial \mathbf{F}_S}{\partial \mathbf{u}_S} \tilde{\mathbf{s}}_0 \quad (\text{B11})$$

655 For the transfer of the moments, the relationship will be different whether the moments are transferred at the undisplaced destination point  $\bar{\cdot}$   
656 or the displaced destination point.

### 657 Moments at the undisplaced destination point

658 In this section, the moments are transferred to the undisplaced destination point. The vector from the undisplaced destination point to the  
659 displaced source is:

$$660 \quad \mathbf{r} = \mathbf{s}_0 + \delta \mathbf{u}_S \quad (\text{B12})$$

661 Introducing Equation B6 and Equation B12 into Equation B2, and temporarily using the “ $\times$ ” notation instead of the tilde notation:

$$662 \quad \mathbf{M}_{D0} + \delta \mathbf{M}_D = \mathbf{M}_{S0} + \delta \mathbf{M}_S + \mathbf{s}_0 \times \mathbf{F}_{S0} + \mathbf{s}_0 \times \delta \mathbf{F}_S + \delta \mathbf{u}_S \times \mathbf{F}_{S0} + \delta \mathbf{u}_S \times \delta \mathbf{F}_S \quad (\text{B13})$$

663 Making use of Equation B8, neglecting the nonlinear term  $(\delta \mathbf{u}_S \times \delta \mathbf{F}_S)$  and reintroducing the tilde notation  $\tilde{\cdot}$  leads to:

$$664 \quad \delta \mathbf{M}_D = \delta \mathbf{M}_S + \tilde{\mathbf{s}}_0 \delta \mathbf{F}_S - \tilde{\mathbf{F}}_{S0} \delta \mathbf{u}_S \quad (\text{B14})$$

665 The Jacobians of the moments at the undisplaced node  $D$  with respect to the displacements at node  $D$  are then obtained by applying the  
666 chain rule to Equation B14:

$$667 \quad \frac{\partial \mathbf{M}_D}{\partial \mathbf{u}_D} = \frac{\partial \mathbf{M}_S}{\partial \mathbf{u}_S} \frac{\partial \mathbf{u}_S}{\partial \mathbf{u}_D} + \frac{\partial \mathbf{M}_S}{\partial \boldsymbol{\theta}_S} \frac{\partial \boldsymbol{\theta}_S}{\partial \mathbf{u}_D} + \tilde{\mathbf{s}}_0 \left[ \frac{\partial \mathbf{F}_S}{\partial \mathbf{u}_S} \frac{\partial \mathbf{u}_S}{\partial \mathbf{u}_D} + \frac{\partial \mathbf{F}_S}{\partial \boldsymbol{\theta}_S} \frac{\partial \boldsymbol{\theta}_S}{\partial \mathbf{u}_D} \right] - \tilde{\mathbf{F}}_{S0} \frac{\partial \mathbf{u}_S}{\partial \mathbf{u}_D}$$

$$668 \quad = \frac{\partial \mathbf{M}_S}{\partial \mathbf{u}_S} + \tilde{\mathbf{s}}_0 \frac{\partial \mathbf{F}_S}{\partial \mathbf{u}_S} - \tilde{\mathbf{F}}_{S0} \quad (\text{B15})$$

669 and

$$670 \quad \frac{\partial \mathbf{M}_D}{\partial \boldsymbol{\theta}_D} = \frac{\partial \mathbf{M}_S}{\partial \boldsymbol{\theta}_S} \frac{\partial \boldsymbol{\theta}_S}{\partial \boldsymbol{\theta}_D} + \frac{\partial \mathbf{M}_S}{\partial \mathbf{u}_S} \frac{\partial \mathbf{u}_S}{\partial \boldsymbol{\theta}_D} + \tilde{\mathbf{s}}_0 \left[ \frac{\partial \mathbf{F}_S}{\partial \boldsymbol{\theta}_S} \frac{\partial \boldsymbol{\theta}_S}{\partial \boldsymbol{\theta}_D} + \frac{\partial \mathbf{F}_S}{\partial \mathbf{u}_S} \frac{\partial \mathbf{u}_S}{\partial \boldsymbol{\theta}_D} \right] - \tilde{\mathbf{F}}_{S0} \frac{\partial \mathbf{u}_S}{\partial \boldsymbol{\theta}_D}$$

$$671 \quad = \frac{\partial \mathbf{M}_S}{\partial \boldsymbol{\theta}_S} - \frac{\partial \mathbf{M}_S}{\partial \mathbf{u}_S} \tilde{\mathbf{s}}_0 + \tilde{\mathbf{s}}_0 \frac{\partial \mathbf{F}_S}{\partial \boldsymbol{\theta}_S} - \tilde{\mathbf{s}}_0 \frac{\partial \mathbf{F}_S}{\partial \mathbf{u}_S} \tilde{\mathbf{s}}_0 + \tilde{\mathbf{F}}_{S0} \tilde{\mathbf{s}}_0 \quad (\text{B16})$$

### 672 Jacobian relationships at the undisplaced destination point

673 Equation B11, Equation B16, and Equation B15 can be gathered in matricial form to relate the different Jacobians between the source point  
674 and the undisplaced destination point:

$$675 \quad \begin{bmatrix} \frac{\partial \mathbf{F}_D}{\partial \mathbf{u}_D} & \frac{\partial \mathbf{F}_D}{\partial \boldsymbol{\theta}_D} \\ \frac{\partial \mathbf{M}_D}{\partial \mathbf{u}_D} & \frac{\partial \mathbf{M}_D}{\partial \boldsymbol{\theta}_D} \end{bmatrix}_{\text{undisplaced}} = \begin{bmatrix} \mathbf{I} & \mathbf{0} \\ \tilde{\mathbf{s}}_0 & \mathbf{I} \end{bmatrix} \begin{bmatrix} \frac{\partial \mathbf{F}_S}{\partial \mathbf{u}_S} & \frac{\partial \mathbf{F}_S}{\partial \boldsymbol{\theta}_S} \\ \frac{\partial \mathbf{M}_S}{\partial \mathbf{u}_S} & \frac{\partial \mathbf{M}_S}{\partial \boldsymbol{\theta}_S} \end{bmatrix} \begin{bmatrix} \mathbf{I} & -\tilde{\mathbf{s}}_0 \\ \mathbf{0} & \mathbf{I} \end{bmatrix} + \begin{bmatrix} \mathbf{0} & \mathbf{0} \\ -\tilde{\mathbf{F}}_{S0} & \tilde{\mathbf{F}}_{S0} \tilde{\mathbf{s}}_0 \end{bmatrix} \quad (\text{B17})$$

### 676 Moments at the displaced destination point

677 In this section, the moments are transferred to the displaced destination point. The vector from the displaced destination point to the displaced  
678 source is:

$$679 \quad \mathbf{r} = \mathbf{s}_0 + \delta \mathbf{u}_S - \delta \mathbf{u}_D = \mathbf{s}_0 - \tilde{\mathbf{s}}_0 \delta \boldsymbol{\theta}_S \quad (\text{B18})$$

680 Introducing Equation B6 and Equation B18 into Equation B2, and temporarily using the “ $\times$ ” notation instead of the tilde notation:

$$681 \quad \mathbf{M}_{D0} + \delta \mathbf{M}_D = \mathbf{M}_{S0} + \delta \mathbf{M}_S + \mathbf{s}_0 \times \mathbf{F}_{S0} + \mathbf{s}_0 \times \delta \mathbf{F}_S - (\mathbf{s}_0 \times \delta \boldsymbol{\theta}_S) \times \mathbf{F}_{S0} - (\mathbf{s}_0 \times \delta \boldsymbol{\theta}_S) \times \delta \mathbf{F}_S \quad (\text{B19})$$

682 Making use of Equation B8, neglecting the nonlinear term  $((\mathbf{s}_0 \times \delta\boldsymbol{\theta}_S) \times \delta\mathbf{F}_S)$ , and reintroducing the tilde notation  $\tilde{\cdot}$  leads to:

$$683 \quad \delta\mathbf{M}_D = \delta\mathbf{M}_S + \tilde{\mathbf{s}}_0 \delta\mathbf{F}_S + \tilde{\mathbf{F}}_{S0} \tilde{\mathbf{s}}_0 \delta\boldsymbol{\theta}_S \quad (\text{B20})$$

684 The Jacobians of the loads at the displaced node  $D$  with respect to the displacements at node  $D$  are then obtained by applying the chain rule  
685 to Equation B20 and making use of the Jacobian of the displacements given on the right of Equation B4.

$$686 \quad \frac{\partial \mathbf{M}_D}{\partial \mathbf{u}_D} = \frac{\partial \mathbf{M}_S}{\partial \mathbf{u}_S} \frac{\partial \mathbf{u}_S}{\partial \mathbf{u}_D} + \frac{\partial \mathbf{M}_S}{\partial \boldsymbol{\theta}_S} \frac{\partial \boldsymbol{\theta}_S}{\partial \mathbf{u}_D} + \tilde{\mathbf{s}}_0 \frac{\partial \mathbf{F}_S}{\partial \mathbf{u}_S}$$

$$687 \quad = \frac{\partial \mathbf{M}_S}{\partial \mathbf{u}_S} + \tilde{\mathbf{s}}_0 \frac{\partial \mathbf{F}_S}{\partial \mathbf{u}_S} \quad (\text{B21})$$

688 and

$$689 \quad \frac{\partial \mathbf{M}_D}{\partial \boldsymbol{\theta}_D} = \frac{\partial \mathbf{M}_S}{\partial \mathbf{u}_S} \frac{\partial \mathbf{u}_S}{\partial \boldsymbol{\theta}_D} + \frac{\partial \mathbf{M}_S}{\partial \boldsymbol{\theta}_S} \frac{\partial \boldsymbol{\theta}_S}{\partial \boldsymbol{\theta}_D} + \tilde{\mathbf{s}}_0 \frac{\partial \mathbf{F}_S}{\partial \boldsymbol{\theta}_D} + \tilde{\mathbf{F}}_{S0} \tilde{\mathbf{s}}_0$$

$$690 \quad = \frac{\partial \mathbf{M}_S}{\partial \boldsymbol{\theta}_S} - \frac{\partial \mathbf{M}_S}{\partial \mathbf{u}_S} \tilde{\mathbf{s}}_0 + \tilde{\mathbf{s}}_0 \frac{\partial \mathbf{F}_S}{\partial \boldsymbol{\theta}_D} + \tilde{\mathbf{F}}_{S0} \tilde{\mathbf{s}}_0$$

$$691 \quad = \frac{\partial \mathbf{M}_S}{\partial \boldsymbol{\theta}_S} - \frac{\partial \mathbf{M}_S}{\partial \mathbf{u}_S} \tilde{\mathbf{s}}_0 + \tilde{\mathbf{s}}_0 \frac{\partial \mathbf{F}_S}{\partial \boldsymbol{\theta}_S} - \tilde{\mathbf{s}}_0 \frac{\partial \mathbf{F}_S}{\partial \mathbf{u}_S} \tilde{\mathbf{s}}_0 + \tilde{\mathbf{F}}_{S0} \tilde{\mathbf{s}}_0 \quad (\text{B22})$$

## 692 Jacobian relationships at the displaced destination point

693 Equation B11, Equation B22, and Equation B21 can be gathered in matricial form to relate the different Jacobians:

$$694 \quad \begin{bmatrix} \frac{\partial \mathbf{F}_D}{\partial \mathbf{u}_D} & \frac{\partial \mathbf{F}_D}{\partial \boldsymbol{\theta}_D} \\ \frac{\partial \mathbf{M}_D}{\partial \mathbf{u}_D} & \frac{\partial \mathbf{M}_D}{\partial \boldsymbol{\theta}_D} \end{bmatrix}_{\text{displaced}} = \begin{bmatrix} \mathbf{I} & \mathbf{0} \\ \tilde{\mathbf{s}}_0 & \mathbf{I} \end{bmatrix} \begin{bmatrix} \frac{\partial \mathbf{F}_S}{\partial \mathbf{u}_S} & \frac{\partial \mathbf{F}_S}{\partial \boldsymbol{\theta}_S} \\ \frac{\partial \mathbf{M}_S}{\partial \mathbf{u}_S} & \frac{\partial \mathbf{M}_S}{\partial \boldsymbol{\theta}_S} \end{bmatrix} \begin{bmatrix} \mathbf{I} & -\tilde{\mathbf{s}}_0 \\ \mathbf{0} & \mathbf{I} \end{bmatrix} + \begin{bmatrix} \mathbf{0} & \mathbf{0} \\ \mathbf{0} & \tilde{\mathbf{F}}_{S0} \tilde{\mathbf{s}}_0 \end{bmatrix} \quad (\text{B23})$$

## 695 B2 Relationships at the displaced destination point for multiple source points

696 We now consider the case where multiple point sources are present. The derivation can be seen as a generalization of the previous case  
697 between two points, but special care is needed **when summing the contributions from the different nodes**. The notations are illustrated in  
Figure B2. The loads at the destination points are obtained as:

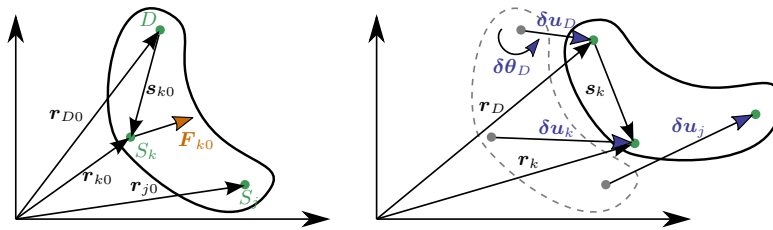


**Figure B2.** Rigid-body kinematics with the loads from multiple source points ( $S_j$ ), transferred to a destination point ( $D$ )

698

$$699 \quad \mathbf{F}_D = \sum_k \mathbf{F}_k \quad (\text{B24})$$

$$700 \quad \mathbf{M}_D = \sum_k \mathbf{M}_k + \tilde{\mathbf{s}}_k \mathbf{F}_k \quad (\text{B25})$$

701 where  $k$  is an index looping over all points of the rigid structure. To shorten notations, we define the vector between the destination point and  
 702 a given point as:

$$703 \quad \mathbf{s}_k = \mathbf{r}_k - \mathbf{r}_D \quad (\text{B26})$$

$$704 \quad \mathbf{s}_{k0} = \mathbf{r}_{k0} - \mathbf{r}_{D0} \quad (\text{B27})$$

705 where  $\mathbf{s}_k$  is the vector between the displaced points and  $\mathbf{s}_{k0}$  is the vector prior to the displacement (at the operating condition). Due to the  
 706 rigid-body assumption, the elementary displacements of the points are related as follows:

$$707 \quad \delta \mathbf{u}_D = \delta \mathbf{u}_j + \tilde{\mathbf{s}}_{j0} \delta \boldsymbol{\theta}_j$$

$$708 \quad \delta \boldsymbol{\theta}_D = \delta \boldsymbol{\theta}_j \quad (\text{B28})$$

709 from which one obtains the following useful relationships:

$$710 \quad \frac{\partial \mathbf{u}_j}{\partial \mathbf{u}_D} = \mathbf{I}, \quad \frac{\partial \boldsymbol{\theta}_j}{\partial \mathbf{u}_D} = \mathbf{O}, \quad \frac{\partial \mathbf{u}_j}{\partial \boldsymbol{\theta}_D} = -\tilde{\mathbf{s}}_{j0}, \quad \frac{\partial \boldsymbol{\theta}_j}{\partial \boldsymbol{\theta}_D} = \mathbf{I}, \quad \frac{\partial \boldsymbol{\theta}_j}{\partial \boldsymbol{\theta}_k} = \mathbf{I} \delta_{jk}, \quad \frac{\partial \boldsymbol{\theta}_j}{\partial \mathbf{u}_k} = \mathbf{O} \quad (\text{B29})$$

711 Using a similar Taylor expansion as for the case with two nodes, the perturbation loads are obtained as:

$$712 \quad \delta \mathbf{F}_D = \sum_k \delta \mathbf{F}_k \quad (\text{B30})$$

$$713 \quad \delta \mathbf{M}_D = \sum_k \delta \mathbf{M}_k + \tilde{\mathbf{s}}_{k0} \delta \mathbf{F}_k + \tilde{\mathbf{F}}_{k0} (\tilde{\mathbf{s}}_{k0} \delta \boldsymbol{\theta}_k) \quad (\text{B31})$$

714 The chain rule for a given quantity of interest ( $Q$ ) is obtained by summing over all the elementary variables:

$$715 \quad dQ = \sum_j \frac{\partial Q}{\partial \mathbf{u}_j} d\mathbf{u}_j + \frac{\partial Q}{\partial \boldsymbol{\theta}_j} d\boldsymbol{\theta}_j \quad (\text{B32})$$

716 For instance, the application of the applying the chain rule to  $\mathbf{F}_D$  and using Equation B30 leads to:

$$717 \quad \frac{\partial \mathbf{F}_D}{\partial \mathbf{u}_D} = \sum_j \frac{\partial \mathbf{F}_D}{\partial \mathbf{u}_j} \frac{\partial \mathbf{u}_j}{\partial \mathbf{u}_D} + \frac{\partial \mathbf{F}_D}{\partial \boldsymbol{\theta}_j} \frac{\partial \boldsymbol{\theta}_j}{\partial \mathbf{u}_D} = \sum_j \sum_k \frac{\partial \mathbf{F}_k}{\partial \mathbf{u}_j} \frac{\partial \mathbf{u}_j}{\partial \mathbf{u}_D} + \frac{\partial \mathbf{F}_k}{\partial \boldsymbol{\theta}_j} \frac{\partial \boldsymbol{\theta}_j}{\partial \mathbf{u}_D} = \sum_j \sum_k \frac{\partial \mathbf{F}_k}{\partial \mathbf{u}_j} \quad (\text{B33})$$

718 Eventually, the Jacobians at the displaced destination node are obtained as:

$$719 \quad \left[ \begin{array}{cc} \frac{\partial \mathbf{F}_D}{\partial \mathbf{u}_D} & \frac{\partial \mathbf{F}_D}{\partial \boldsymbol{\theta}_D} \\ \frac{\partial \mathbf{M}_D}{\partial \mathbf{u}_D} & \frac{\partial \mathbf{M}_D}{\partial \boldsymbol{\theta}_D} \end{array} \right]_{\text{displaced}} = \sum_j \left\{ \sum_k \left( \left[ \begin{array}{cc} \mathbf{I} & \mathbf{0} \\ \tilde{\mathbf{s}}_{k0} & \mathbf{I} \end{array} \right] \left[ \begin{array}{cc} \frac{\partial \mathbf{F}_k}{\partial \mathbf{u}_j} & \frac{\partial \mathbf{F}_k}{\partial \boldsymbol{\theta}_j} \\ \frac{\partial \mathbf{M}_k}{\partial \mathbf{u}_j} & \frac{\partial \mathbf{M}_k}{\partial \boldsymbol{\theta}_j} \end{array} \right] \left[ \begin{array}{cc} \mathbf{I} & -\tilde{\mathbf{s}}_{j0} \\ \mathbf{0} & \mathbf{I} \end{array} \right] \right) + \left[ \begin{array}{cc} \mathbf{0} & \mathbf{0} \\ \mathbf{0} & \tilde{\mathbf{F}}_{j0} \tilde{\mathbf{s}}_{j0} \end{array} \right] \right\} \quad (\text{B34})$$

## 720 Appendix C: Verification of the linear models

721 In this section, we supplement the results given in Section 3.3.3 by showing free-decay results without hydrodynamics (no added mass,  
 722 damping, hydrostatics). We In Figure C1, we show results with the structure only in, and results with the structure and moorings are reported  
 723 in Figure C2. These results also include the nonlinear WELIB formulation. A strong agreement is found between the nonlinear OpenFAST  
 724 and WELIB models, and between the linear OpenFAST and WELIB models. The yaw degree of freedom appears to be more challenging  
 725 to capture for the linear models. We recall that OpenFAST and WELIB use different definition of the transformation matrices between the  
 726 degrees of freedom, which results in different structural dynamic equations.



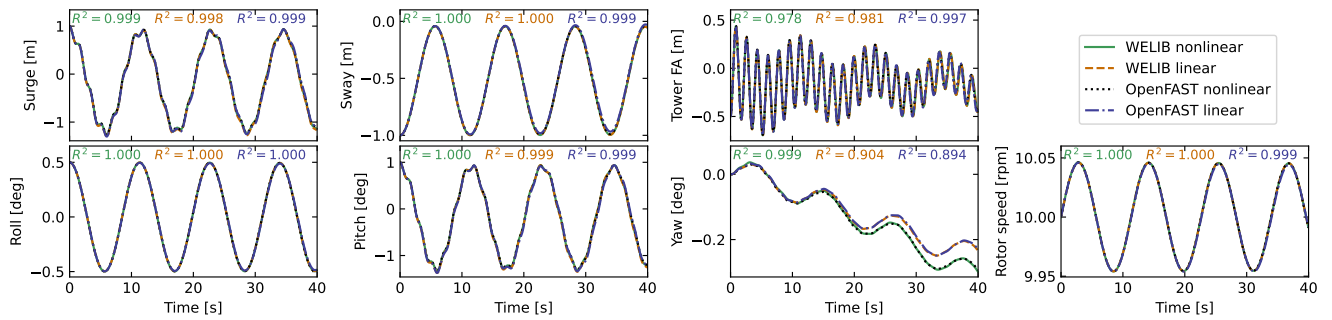


**Figure C1.** Free decay of the structure using nonlinear and linear models for a case including only the structure (no moorings, no hydrodynamics). Time series of the main  $\text{DOFs}$ .

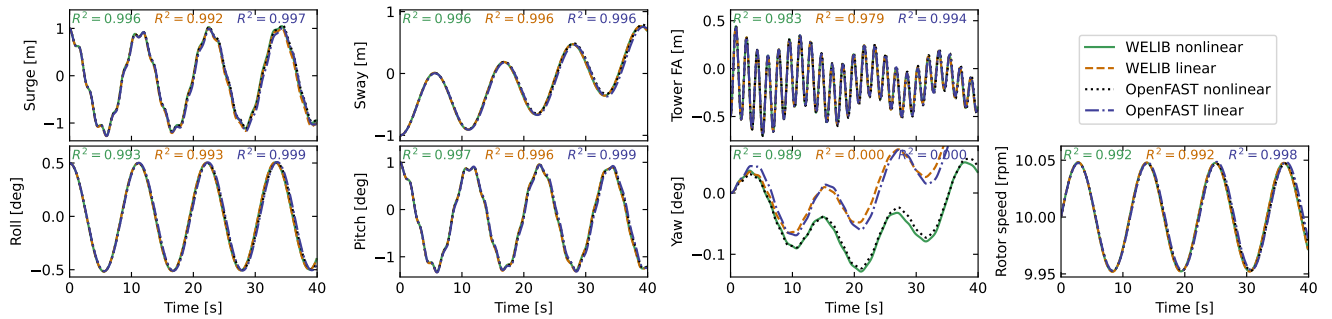


**Figure C2.** Free decay of the structure using nonlinear and linear models for a case including moorings (no hydrodynamics). Time series of the main  $\text{DOFs}$ .

## 727 Appendix D: Computation of section loads

728 In this section, we describe the nonlinear calculation procedure used in Section 3.6.2 to assess the section loads along the tower based on  
 729 estimates of the structure kinematics and the loads at the tower top. For conciseness, in this appendix, we use  $x$  and  $z$  for the coordinates  
 730 along the tower fore-aft and tower height, respectively, instead of  $x_T$  and  $z_T$ .

### 731 D1 Tower fore-aft bending moment and shear force

732 The fore-aft and side-side ~~loads are computed~~ moments are computed in the same way, ~~therefore~~; therefore, this section focuses on the  
 733 fore-aft direction. The sectional fore-aft bending moment at a given tower height  $z$  is determined as:

$$734 \mathcal{M}_y(z) = \mathcal{M}_{y,\text{top}} - \int_z^{L_T} S_x(z') dz' \quad (\text{D1})$$

735 ~~here~~ Here,  $\mathcal{M}_{y,\text{top}}$  is the fore-aft bending moment at the tower top, and  $S_x$  is the shear force in the  $x$  direction, obtained as:

$$736 S_x(z) = \int_z^{L_T} p_{x,\text{all}}(z') dz' \quad (\text{D2})$$

737 where  $p_{x,\text{all}}$  is the force per unit length acting on the tower section in the fore-aft direction, including contributions from the external loads  
738 (aerodynamic loads on the structure), inertial loads due to the acceleration of the structure (including gravity), and nonlinear correction terms  
739 from the loads in the  $z$  direction ( $p - \Delta$  effect, including self-weight effects). The different contributions are written as follows:

$$740 \quad p_{x,\text{all}} = p_{x,\text{ext}} + p_{x,\text{corr}} - p_{x,\text{acc}} \quad (\text{D3})$$

741 In this work, we neglect the external loads on the tower,  $p_{x,\text{ext}} = 0$  (aerodynamic loads on the tower are typically small relative to rotor-thrust  
742 loads for an operating wind turbine). The acceleration contribution is  $p_{x,\text{acc}} = -m(z)(a_{x,\text{struct}}(z) - a_{x,\text{grav}})$ , where  $m$  is the mass per length  
743 along the beam, and  $a_{x,\text{struct}}(z)$  is the acceleration of the section, determined based on the rigid-body acceleration of the floater and the elastic  
744 motion of the tower ( $\dot{q}_T$  and  $\ddot{q}_T$ ), and  $a_{x,\text{grav}}$  is the acceleration of gravity in the  $x$  direction. The  $p - \Delta$  correction term due to the vertical  
745 loading is computed as (see Branlard (2019)):

$$746 \quad p_{x,\text{corr}} = \frac{d^2\Phi}{dz^2} \left[ \int_z^L p_z dx' + \sum_{z_k \geq z} \mathcal{F}_{z,k} \right] - \frac{d\Phi}{dz} \left[ p_z + \sum_k \mathcal{F}_{z,k} \delta(z - z_k) \right] \quad (\text{D4})$$

747 where  $p_z$  is the vertical load per unit length (mostly consisting of the self-weight),  $\mathcal{F}_{z,k}$  is the  $k$ -th vertical force acting at point  $z_k$ , and  
748  $\delta$  is the Dirac function, and  $\Phi$  is the shape function used to describe the tower displacement field (see Section 2.3.3). In our case, only the  
749 vertical force acting on top of the tower is present,  $z_1 = L_T$  and  $\mathcal{F}_{z,1} = \mathcal{F}_{z,\text{top}}$ . The procedure is similar to compute the section loads in the  
750  $y$  direction (using the  $p - \Delta$  correction as well) is similar.

## 751 D2 Tower and RNA-rotor-nacelle assembly kinematics

752 The determination of the tower section loads requires a knowledge of the tower kinematics, to compute  $\mathbf{a}_{\text{struct}}$ , and the RNA of the  
753 rotor-nacelle assembly (RNA) kinematics, to compute the inertial contribution to the tower-top loads (see Section D3). The position, linear  
754 velocity, linear acceleration, rotational speed, and rotational acceleration of the floater (point  $F$ , body  $f$ ) are given respectively by:

$$755 \quad \mathbf{r}_F = \{x, y, z\}_i, \quad \mathbf{v}_F = \{\dot{x}, \dot{y}, \dot{z}\}_i, \quad \mathbf{a}_F = \{\ddot{x}, \ddot{y}, \ddot{z}\}_i, \quad (\text{D5})$$

$$756 \quad \boldsymbol{\omega}_f = \{\dot{\phi}_z, \dot{\phi}_y, \dot{\phi}_x\}_i, \quad \dot{\boldsymbol{\omega}}_f = \{\ddot{\phi}_z, \ddot{\phi}_y, \ddot{\phi}_x\}_i \quad (\text{D6})$$

757 where the notation  $i$  indicates that the coordinates of the vector are expressed in the inertial coordinate system. The transformation matrix  
758 from the floater to the inertial frame is obtained as  $\mathbf{R}_{f2i} = \mathbf{R}(\phi_x, \phi_y, \phi_z)$ , where  $\mathbf{R}$  is a function computing the rotation matrix. The tower  
759 base (point  $T$ , body  $t$ ) kinematics are obtained from the floater using rigid-body-motion using rigid-body kinematics:

$$760 \quad \mathbf{r}_T = \mathbf{r}_F + \mathbf{r}_{FT}, \quad (\text{D7})$$

$$761 \quad \mathbf{v}_T = \mathbf{v}_F + \boldsymbol{\omega}_f \times \mathbf{r}_{FT}, \quad (\text{D8})$$

$$762 \quad \mathbf{a}_T = \mathbf{a}_F + \boldsymbol{\omega}_f \times (\boldsymbol{\omega}_f \times \mathbf{r}_{FT}) + \dot{\boldsymbol{\omega}}_f \times \mathbf{r}_{FT}, \quad (\text{D9})$$

$$763 \quad \boldsymbol{\omega}_t = \boldsymbol{\omega}_f, \quad \dot{\boldsymbol{\omega}}_t = \dot{\boldsymbol{\omega}}_f, \quad \mathbf{R}_{t2i} = \mathbf{R}_{f2i} \quad (\text{D10})$$

764 where  $\mathbf{r}_{FT}$  is the vector from the floater point to the tower base. The kinematics of a given tower section (point  $S$ , at height  $z$ ) are given by:

$$765 \quad \mathbf{r}_S = \mathbf{r}_T + \mathbf{r}_{TS} = \mathbf{r}_T + \mathbf{r}_{TS_0} + \mathbf{u}_S, \quad (\text{D11})$$

$$766 \quad \mathbf{v}_S = \mathbf{v}_T + \boldsymbol{\omega}_t \times \mathbf{r}_{TS} + \dot{\mathbf{u}}_S, \quad (\text{D12})$$

$$767 \quad \mathbf{a}_S = \mathbf{a}_T + \boldsymbol{\omega}_t \times (\boldsymbol{\omega}_t \times \mathbf{r}_{TS}) + \dot{\boldsymbol{\omega}}_t \times \mathbf{r}_{TS} + 2\boldsymbol{\omega}_t \times \dot{\mathbf{u}}_S + \ddot{\mathbf{u}}_S, \quad (\text{D13})$$

$$768 \quad \boldsymbol{\omega}_s = \boldsymbol{\omega}_t + \boldsymbol{\omega}_{ts}, \quad (\text{D14})$$

$$769 \quad \dot{\boldsymbol{\omega}}_s = \dot{\boldsymbol{\omega}}_t + \dot{\boldsymbol{\omega}}_{ts} + \boldsymbol{\omega}_t \times \boldsymbol{\omega}_{ts}, \quad (\text{D15})$$

770 where  $\mathbf{r}_{TS_0} = z\hat{\mathbf{z}}_t$  is the vector from the tower base to the undeflected section,  $\mathbf{u}_S$ ,  $\dot{\mathbf{u}}_S$ ,  $\ddot{\mathbf{u}}_S$  are the elastic motions of the section computed  
771 based on the shape function and the generalized coordinates, e.g.,  $\mathbf{u}_S(z) = \sum_j q_{t,j} \boldsymbol{\Phi}_j = q_t \boldsymbol{\Phi}(z) \hat{\mathbf{x}}_t$  (see e.g., Branlard and Geisler (2022)).

772 We note that OpenFAST also includes a vertical motion [associated with the deflection](#) (referred to as a ‘‘geometric nonlinearity’’) [associated](#)  
773 [with the deflection](#), which we [are currently neglecting](#) in this work. The transformation matrix from the section to the tower is

774  $\mathbf{R}_{s2t} = \mathbf{R}(-u'_{S,y}, u'_{S,x}, 0)$ , where  $u_{S,y}$  and  $u_{S,x}$  are the components of  $\mathbf{u}_S$  in the tower coordinate system, and the prime notation indicates  
775 the differentiation with respect to  $z$ . The rotation speed and acceleration of the tower section with respect to the tower base are:

$$776 \quad \boldsymbol{\omega}_{ts} = \{\dot{u}'_{S,y}, \dot{u}'_{S,x}, 0\}_t, \quad \dot{\boldsymbol{\omega}}_{ts} = \{\ddot{u}'_{S,y}, \ddot{u}'_{S,x}, 0\}_t \quad (\text{D16})$$

777 The kinematics of the tower-top point and nacelle (point  $N$ , body  $n$ ) are taken from the last section node (point  $S$  with  $z = L_T$ ). Yawing,  
778 tilting, and rolling of the tower top would change the orientation matrix, rotational velocity, and rotational acceleration of the nacelle. These  
779 kinematics are omitted here for conciseness. The kinematics of the center of mass of the RNA (point  $G$ ) are obtained using rigid-body  
780 kinematics, identical to what was used between point  $F$  and  $T$ .

### 781 **D3 Tower-top loads**

782 The tower-top loads are computed as follows:

$$783 \quad \mathcal{F}_{\text{top}} = \mathcal{F}_{\text{aero}} - \mathcal{F}_{\text{inertia}} \quad (\text{D17})$$

$$784 \quad \mathcal{M}_{\text{top}} = \mathcal{M}_{\text{aero}} - \mathcal{M}_{\text{inertia}} \quad (\text{D18})$$

785 where the aerodynamic loads are transferred to the tower top and where the inertial loads from the rigid-body RNA are:

$$786 \quad \mathcal{F}_{\text{inertia}} = M_{\text{RNA}}(\mathbf{a}_G - \mathbf{g}) \quad (\text{D19})$$

$$787 \quad \mathcal{M}_{\text{inertia}} = \mathbf{r}_{NG} \times \mathcal{F}_{\text{inertia}} + \mathbf{J}_G \cdot \dot{\boldsymbol{\omega}}_n + \boldsymbol{\omega}_n \times (\mathbf{J}_G \cdot \boldsymbol{\omega}_n) \quad (\text{D20})$$

788 where:  $\mathbf{r}_{NG}$  is the vector from the tower top to the center of mass of the RNA,  $M_{\text{RNA}}$  is the mass of the RNA,  $\mathbf{J}_G$  is the inertia tensor of the  
789 RNA at its center of mass,  $\mathbf{a}_G$  is the linear acceleration of the center of mass of the RNA,  $\boldsymbol{\omega}_n$  is the rotational acceleration of the RNA, [and](#)  
790  $\dot{\boldsymbol{\omega}}_n$  is the rotational acceleration of the nacelle. The load calculation is first done in the coordinate system of the nacelle  $\bar{\mathbf{r}}$  and then transferred  
791 to the coordinate system of the tower where Equation D1 is defined.

## 792 **References**

- 793 Abbas, N., Zalkind, D., Pao, L., and Wright, A.: A Reference Open-Source Controller for Fixed and Floating Offshore Wind Turbines, *Wind*  
794 *Energy Science Discussions*, 2021, 1–33, <https://doi.org/10.5194/wes-2021-19>, 2021.
- 795 Auger, F., Hilairet, M., Guerrero, J. M., Monmasson, E., Orlowska-Kowalska, T., and Katsura, S.: Industrial Applications of the Kalman  
796 Filter: A Review, *IEEE Transactions on Industrial Electronics*, 60, 5458–5471, <https://doi.org/10.1109/TIE.2012.2236994>, 2013.
- 797 Bilbao, J., Lourens, E.-M., Schulze, A., and Ziegler, L.: Virtual sensing in an onshore wind turbine tower using a Gaussian process latent  
798 force model, *Data-Centric Engineering*, 3, <https://doi.org/10.1017/dce.2022.38>, 2022.
- 799 Bossanyi, E. A.: Individual Blade Pitch Control for Load Reduction, *Wind Energy*, 6, 119–128, <https://doi.org/10.1002/we.76>, 2003.
- 800 Bottasso, C. and Croce, A.: Cascading Kalman Observers of Structural Flexible and Wind States for Wind Turbine Control, Tech. rep.,  
801 Dipartimento di Ingegneria Aerospaziale, Politecnico di Milano, Milano, Italy, Scientific Report DIA-SR 09-02, 2009.
- 802 Boukhezzar, B. and Siguerdidjane, H.: Nonlinear Control of a Variable-Speed Wind Turbine Using a Two-Mass Model, *IEEE Transactions*  
803 *on Energy Conversion*, 26, 149–162, <https://doi.org/10.1109/TEC.2010.2090155>, 2011.
- 804 Branlard, E.: Flexible multibody dynamics using joint coordinates and the Rayleigh-Ritz approximation: The general framework behind and  
805 beyond Flex, *Wind Energy*, 22, 877–893, <https://doi.org/10.1002/we.2327>, 2019.
- 806 Branlard, E.: wtDigiTwin GitHub repository <https://github.com/NREL/wtDigiTwin> <https://doi.org/10.5281/zenodo.8048549> Last accessed  
807 June 2023, 2023a.
- 808 Branlard, E.: WELIB, Wind Energy Library, GitHub repository <http://github.com/eBranlard/welib/>, <https://doi.org/10.5281/zenodo.8048349>  
809 Last accessed June 2023, 2023b.
- 810 Branlard, E. and Geisler, J.: A symbolic framework for flexible multibody systems applied to horizontal-axis wind turbines, *Wind Energy*  
811 *Science*, 2022.
- 812 Branlard, E., Giardina, D., and Brown, C. S. D.: Augmented Kalman filter with a reduced mechanical model to estimate tower loads on  
813 a land-based wind turbine: a step towards digital-twin simulations, *Wind Energy Science*, 5, 1155–1167, [https://doi.org/10.5194/wes-5-](https://doi.org/10.5194/wes-5-1155-2020)  
814 [1155-2020](https://doi.org/10.5194/wes-5-1155-2020), 2020a.
- 815 Branlard, E., Jonkman, J., Dana, S., and Doubrawa, P.: A digital twin based on OpenFAST linearizations for real-time load and fatigue esti-  
816 mation of land-based turbines, *Journal of Physics: Conference Series*, 1618, 022 030, <https://doi.org/10.1088/1742-6596/1618/2/022030>,  
817 2020b.
- 818 Castella, X. T.: Operations and maintenance costs for offshore wind farm analysis and strategies to reduce O&M costs, Master’s thesis,  
819 Universitat Politècnica de Catalunya, and National Taiwan University of Science and Technology, 2020.
- 820 Cosack, N.: Fatigue Load Monitoring with Standard Wind Turbine Signals, Ph.D. thesis, Universität Stuttgart, 2010.
- 821 Dimitrov, N., Kelly, M. C., Vignaroli, A., and Berg, J.: From wind to loads: wind turbine site-specific load estimation with surrogate models  
822 trained on high-fidelity load databases, *Wind Energy Science*, 3, 767–790, <https://doi.org/10.5194/wes-3-767-2018>, 2018.
- 823 Eftekhar Azam, S., Chatzi, E., and Papadimitriou, C.: A dual Kalman filter approach for state estimation via output-only acceleration mea-  
824 surements, *Mechanical Systems and Signal Processing*, 60-61, 866 – 886, [https://doi.org/https://doi.org/10.1016/j.ymssp.2015.02.001](https://doi.org/10.1016/j.ymssp.2015.02.001),  
825 2015.
- 826 Evans, M., Han, T., and Shuchun, Z.: Development and validation of real time load estimator on Goldwind 6 MW wind turbine, *Journal of*  
827 *Physics: Conference Series*, 1037, 032 021, <https://doi.org/10.1088/1742-6596/1037/3/032021>, 2018.

828 Iliopoulos, A., Shirzadeh, R., Weijtjens, W., Guillaume, P., Hemelrijck, D. V., and Devriendt, C.: A modal decomposition and expansion  
829 approach for prediction of dynamic responses on a monopile offshore wind turbine using a limited number of vibration sensors, *Mechanical*  
830 *Systems and Signal Processing*, 68-69, 84–104, <https://doi.org/https://doi.org/10.1016/j.ymsp.2015.07.016>, 2016.

831 Jacquelin, E., Bennani, A., and Hamelin, P.: Force reconstruction: analysis and regularization of a deconvolution problem, *Journal of Sound*  
832 *and Vibration*, 265, 81 – 107, [https://doi.org/https://doi.org/10.1016/S0022-460X\(02\)01441-4](https://doi.org/https://doi.org/10.1016/S0022-460X(02)01441-4), 2003.

833 Jonkman, B. and Buhl, M.: *TurbSim User’s Guide*, Tech. Rep. NREL/TP-500-39797, National Renewable Energy Laboratory, Golden,  
834 Colorado, USA, <https://doi.org/10.2172/965520>, 2006.

835 Jonkman, B., Mudafort, R. M., Platt, A., Branlard, E., Sprague, M., Jonkman, J., Vijayakumar, G., Buhl, M., Ross, H., Bortolotti, P., Masciola,  
836 M., Ananthan, S., Schmidt, M. J., Rood, J., Damiani, R., Mendoza, N., Hall, M., and Corniglioni, R.: OpenFAST v3.4.1. Open-source wind  
837 turbine simulation tool, available at <http://github.com/OpenFAST/OpenFAST/>, <https://doi.org/10.5281/zenodo.7632926>, 2023.

838 Jonkman, J. M. and Jonkman, B. J.: FAST modularization framework for wind turbine simulation: full-system linearization, *Journal of*  
839 *Physics: Conference Series*, 753, 082 010, <https://doi.org/10.1088/1742-6596/753/8/082010>, 2016.

840 Jonkman, J. M., Wright, A. D., Hayman, G. J., and Robertson, A. N.: Full-System Linearization for Floating Offshore Wind Turbines in  
841 OpenFAST, vol. ASME 2018 1st International Offshore Wind Technical Conference of *International Conference on Offshore Mechanics*  
842 *and Arctic Engineering*, [https://doi.org/10.1115/IOWTC2018-1025\\_v001T01A028](https://doi.org/10.1115/IOWTC2018-1025_v001T01A028), 2018.

843 Jonkman, J. M., Branlard, E., and Jasa, J. P.: Influence of wind turbine design parameters on linearized physics-based models in OpenFAST,  
844 *Wind Energy Science*, 7, 559–571, <https://doi.org/10.5194/wes-7-559-2022>, 2022.

845 Kalman, R. E.: A new approach to linear filtering and prediction problems, *Journal of Basic Engineering*, 12, 35–45, 1960.

846 Kamel, O., Kretschmer, M., Pfeifer, S., Luhmann, B., Hauptmann, S., and Bottasso, C.: Data-driven virtual sensor for online loads estimation  
847 of drivetrain of wind turbines, *Forschung im Ingenieurwesen*, pp. 1–8, <https://doi.org/10.1007/s10010-023-00615-4>, 2023.

848 Lourens, E., Reynders, E., Roeck, G. D., Degrande, G., and Lombaert, G.: An augmented Kalman filter for force identification in structural  
849 dynamics, *Mechanical Systems and Signal Processing*, 27, 446–460, 2012.

850 Ma, C.-K. and Ho, C.-C.: An inverse method for the estimation of input forces acting on non-linear structural systems, *Journal of Sound and*  
851 *Vibration*, 275, 953 – 971, [https://doi.org/https://doi.org/10.1016/S0022-460X\(03\)00797-1](https://doi.org/https://doi.org/10.1016/S0022-460X(03)00797-1), 2004.

852 Mehlan, F., R. Nejad, A., and Gao, Z.: Digital Twin Based Virtual Sensor for Online Fatigue Damage Monitoring in Offshore Wind Turbine  
853 Drivetrains, *Journal of Offshore Mechanics and Arctic Engineering*, 144, 1–9, <https://doi.org/10.1115/1.4055551>, 2022.

854 Mehlan, F., Keller, J., and R. Nejad, A.: Virtual sensing of wind turbine hub loads and drivetrain fatigue damage, *Forschung im Ingenieur-*  
855 *wesen*, pp. 1–12, <https://doi.org/10.1007/s10010-023-00627-0>, 2023.

856 Mendez Reyes, H., Kanev, S., Doekemeijer, B., and van Wingerden, J.-W.: Validation of a lookup-table approach to modeling turbine fatigue  
857 loads in wind farms under active wake control, *Wind Energy Science*, 4, 549–561, <https://doi.org/10.5194/wes-4-549-2019>, 2019.

858 Noppe, N., Iliopoulos, A., Weijtjens, W., and Devriendt, C.: Full load estimation of an offshore wind turbine based on SCADA and ac-  
859 celerometer data, *Journal of Physics: Conference Series*, 753, 072 025, <https://doi.org/10.1088/1742-6596/753/7/072025>, 2016.

860 Schröder, L., Dimitrov, N. K., Verelst, D. R., and Sørensen, J. A.: Wind turbine site-specific load estimation using artificial neural networks  
861 calibrated by means of high-fidelity load simulations, *Journal of Physics: Conference Series*, 1037, 062 027, [https://doi.org/10.1088/1742-](https://doi.org/10.1088/1742-6596/1037/6/062027)  
862 [6596/1037/6/062027](https://doi.org/10.1088/1742-6596/1037/6/062027), 2018.

863 Selvam, K., Kanev, S., van Wingerden, J. W., van Engelen, T., and Verhaegen, M.: Feedback–feedforward individual pitch control for wind  
864 turbine load reduction, *International Journal of Robust and Nonlinear Control*, 19, 72–91, <https://doi.org/10.1002/rnc.1324>, 2009.

865 Song, Z., Hackl, C., Anand, A., Thommessen, A., Petzschmann, J., Kamel, O., Braunbehrens, R., Kaifel, A., Roos, C., and  
866 Hauptmann, S.: Digital Twins for the Future Power System: An Overview and a Future Perspective, *Sustainability*, 15, 5259,  
867 <https://doi.org/10.3390/su15065259>, 2023.

868 Stiesdal Offshore: The TetraSpar full scale demonstration project, [https://www.stiesdal.com/offshore-technologies/  
869 the-tetraspar-full-scale-demonstration-project/](https://www.stiesdal.com/offshore-technologies/the-tetraspar-full-scale-demonstration-project/), 2022.

870 Zarchan, P. and Musoff, H.: *Fundamentals of Kalman filtering : a practical approach*, Fourth Edition, AIAA, Progress in astronautics and  
871 aeronautics, 2015.

872 Ziegler, L., Smolka, U., Cosack, N., and Muskulus, M.: Brief communication: Structural monitoring for lifetime extension of offshore wind  
873 monopiles: can strain measurements at one level tell us everything?, *Wind Energy Science*, 2, 469–476, [https://doi.org/10.5194/wes-2-  
874 469-2017](https://doi.org/10.5194/wes-2-469-2017), 2017.